The Structure and Dynamics of An Active Galactic Nucleus Torus

Perez Beaupuits, J.P.; Wada, K.; Spaans, M.

Published in:
Astrophysical Journal

DOI:
10.1088/0004-637X/730/1/48

The Astrophysical Journal, 730:48 (18pp), 2011 March 20 doi:10.1088/0004-637X/730/1/48

THE STRUCTURE AND DYNAMICS OF AN ACTIVE GALACTIC NUCLEUS TORUS: CO LINE PREDICTIONS FOR ALMA FROM THREE-DIMENSIONAL HYDRODYNAMICAL SIMULATIONS WITH X-RAY-DRIVEN CHEMISTRY

J. P. Pérez-Beaupuits[1,2,4], K. Wada[3,5], and M. Spaans[2]
[1] Max-Planck-Institut für Radioastronomie, Auf dem Hügel 69, 53121 Bonn, Germany; jp@mpifr.de
[2] Kapteyn Astronomical Institute, Rijksuniversiteit Groningen, 9747 AD Groningen, The Netherlands; spaans@astro.rug.nl
[3] Graduate School of Science and Engineering, Kagoshima University, Kagoshima 890-0065, Japan; wada@sci.kagoshima-u.ac.jp
Received 2010 November 29; accepted 2011 January 19; published 2011 March 3

ABSTRACT

Several attempts have been made to model the mass distribution and dynamical evolution of the circumnuclear gas in active galactic nuclei (AGNs). However, chemical evolution is not included in detail in three-dimensional (3D) hydrodynamic simulations. The X-ray radiation from the AGN can drive the gas chemistry and affect the thermodynamics, as well as the excitation of the interstellar medium. Therefore, we estimate the effects (on chemical abundances and excitation) of X-ray irradiation by the AGN for atomic and molecular gas in a 3D hydrodynamic model of an AGN torus. We obtain the abundances of various species from an X-ray chemical model. A 3D radiative transfer code estimates the level populations, which result in line intensity maps. Predictions for the CO $J = 1 \rightarrow 0$ to $J = 9 \rightarrow 8$ lines indicate that mid-J CO lines are excellent probes of density and dynamics in the central ($\lesssim$60 pc) region of the AGN in contrast to the low-J CO lines. Analysis of the $X_{\rm CO}/\alpha$ conversion factors shows that only the higher J CO lines can be used for gas mass determination in AGN tori. The [C II] 158 μm emission traces mostly the hot ($T_k > 1000$ K) central region of the AGN torus. The [C II] 158 μm line will be useful for ALMA observations of high-redshift ($z \gtrsim 1$) AGNs. The spatial scales ($\geqslant$0.25 pc) probed with our simulations match the size of the structures that ALMA will resolve in nearby ($\leqslant$45 Mpc at 0.″01) galaxies.

Key words: galaxies: evolution – galaxies: ISM – methods: numerical

Online-only material: color figures

1. INTRODUCTION

The formation and growth of a central black hole and its interaction with intense star-forming regions is one of the topics most debated in the context of galaxy evolution. There is observational evidence for a common physical process from which most active galactic nuclei (AGNs) and starbursts originate (e.g., Soltan 1982; Magorrian et al. 1998; Ferrarese & Merritt 2000; Graham et al. 2001; Häring & Rix 2004). A plausible scenario considers that starbursts, supermassive black hole (SMBH) growth, and the formation of red elliptical and submillimeter galaxies (SMGs) are connected through an evolutionary sequence caused by mergers between gas-rich galaxies (Hopkins et al. 2006, 2008; Tacconi et al. 2008; Narayanan et al. 2009, 2010). In this scenario, the starbursts and (X-ray producing) AGNs seem to be coeval, and the interaction process between them (phase d and e in Figure 1 of Hopkins et al. 2008), which dominates the formation and emission of molecular gas, is one of the long-standing issues concerning active galaxies.

Numerous molecules tracing different (AGN and starburst driven) gas chemistries have been detected in Galactic and (active) extragalactic environments. Studies have shown that the chemical differentiation observed within Galactic molecular clouds is also seen at larger (~100 pc) scales in nearby galaxies (e.g., Henkel et al. 1987; Nguyen-Q-Rieu et al. 1991; Martín et al. 2003; Usero et al. 2004; Tacconi et al. 2008; Pérez-Beaupuits et al. 2007, 2009, 2010; Baan et al. 2010; van der Werf et al. 2010).

The evolution of the interstellar medium (ISM) in the inner 100 pc region around a $10^8\,M_\odot$ SMBH was investigated by Wada & Norman (2002, hereafter WN02) using three-dimensional (3D) Euler-grid hydrodynamic simulations. They took into account self-gravity of the gas, radiative cooling, and heating due to supernovae (SNe). A clumpy and filamentary torus-like structure was found to be reproduced on a scale of tens of parsec around the SMBH, with highly inhomogeneous ambient density and temperature, and turbulent velocity field. Their results indicated that AGNs could be obscured by the circumnuclear material. This represents theoretical support for observational evidence showing that some AGNs are obscured by nuclear starbursts (e.g., Levenson et al. 2001, 2007; Ballantyne 2008, and references therein).

Several attempts have been made to estimate the molecular line emission from the nuclear region in these 3D hydrodynamic simulations, and to compare the results with observational data. For instance, Wada & Tomisaka (2005, hereafter WT05) derived molecular line intensities emitted from the nuclear starburst region around an SMBH in an AGN. They used the 3D hydrodynamic simulations (density, temperature, and velocity field data) of the multi-phase gas modeled by WN02 as input for 3D non-LTE radiative transfer calculations of ^{12}CO and ^{13}CO lines. They found that the CO-to-H_2 conversion factor (X-factor) is not uniformly distributed in the central 100 pc and the X-factor for ^{12}CO $J = 1 \rightarrow 0$ is not constant with density in contrast with the ^{12}CO $J = 3 \rightarrow 2$ line. Similarly, the role of the HCN and HCO^+ high-density tracers in the inhomogeneous molecular torus of WN02 was studied by Yamada et al. (2007, hereafter YWT07). These non-LTE radiative transfer calculations suggested a complicated excitation state of the rotational lines of HCN (with maser

[4] Research Fellow of the Alexander von Humboldt Foundation.
[5] Visiting researcher, Research Center for Space and Cosmic Evolution, Ehime University, Ehime, Japan.

action) and HCO^+, regardless of the spatially uniform chemical abundance assumed.

However, all these previous attempts to estimate the molecular line emissions from the central 100 pc of an AGN leave room for improvements. First of all, the radiative cooling in the simulations by WN02 are not consistent with the chemical abundances in the cold and dense gas because (collisional) formation and (radiative) destruction of H_2 by far-ultraviolet (FUV) radiation was not included. Therefore, the cold and dense gas in the simulations by WN02 does not necessarily represent the dusty molecular gas phase around an AGN.

Hence, in order to study the distribution and structures of the various density regimes of the H_2 gas, the 3D hydrodynamic simulations of WN02 were extended by Wada et al. (2009, hereafter WPS09) to solve the nonequilibrium chemistry of hydrogen molecules along with the hydrodynamics. The formation of H_2 on dust and its radiative destruction by FUV radiation from massive stars are also included in the model by WPS09. This allows us to track the evolution of molecular hydrogen and its interplay with the H I phase in the central $64 \times 64 \times 32$ pc region. Thus, the radiative cooling in the model by WPS09 is more consistent with the chemical abundances expected in the cold ISM in comparison with the models by WN02. Different SN rates and strengths of the uniform FUV field were also explored in order to study their effects on the structures of molecular gas.

On the other hand, the inhomogeneous density and temperature structures observed in the 3D hydrodynamic models are not the only factors that drive molecular abundances and excitation conditions of molecular lines. There is observational and theoretical evidence in the literature that supports different chemical evolution scenarios due to X-ray and UV radiation from the central AGN and circumnuclear starburst, as well as mechanical heating produced by turbulence and SNe (e.g., Kohno et al. 2001, 2007; Kohno 2005; Imanishi & Wada 2004; Imanishi et al. 2006a, 2006b; Imanishi & Nakanishi 2006; Aalto et al. 2007; Meijerink et al. 2007; García-Burillo et al. 2007; Loenen et al. 2008; García-Burillo et al. 2008; Pérez-Beaupuits et al. 2009). The strong UV and X-ray radiation from the AGN and accretion disk could affect both the dynamics and excitation of the molecular gas (e.g., Ohsuga & Umemura 2001a, 2001b; Meijerink et al. 2007; van der Werf et al. 2010). However, the radiation field from the AGN itself was not taken into account in the earlier estimates of molecular line emissions from hydrodynamical simulations.

A preliminary estimate of the potential effects of hard X-rays ($E > 1$ keV) on the molecular gas was done by WPS09 using the X-ray dissociated region (XDR) models of Meijerink & Spaans (2005). It was found that XDR chemistry may change the distribution of H_2 around an AGN, if X-ray effects are explicitly included in the hydrodynamic model. The X-ray chemistry depends mainly on H_X/n, where H_X is the X-ray energy deposition rate and n is the number density of the gas (Maloney et al. 1996). Although the H_2 abundance is robust in a clumpy medium like the one found in the hydrodynamical models, the temperature of the gas affected by an X-ray flux is expected to be a factor of $\sim$5 higher than that found in standard models of a photon-dominated region (PDR; e.g., Hollenbach & Tielens 1999) for $\log(H_X)/n > 26$ (Meijerink et al. 2007). This is because the ionization heating by X-rays is more efficient than photoelectric emission by dust grains.

Other molecular and atomic lines have also been suggested as tracers of the AGN and starburst activity in nearby galaxies ($z < 1$) as well as in high ($z \geqslant 1$) redshift galaxies. Spaans & Meijerink (2008) studied the possibility of using ^{12}CO and H_2 emission lines to trace a young population of accreting massive ($\geqslant 10^6\ M_\odot$) black holes at redshifts $z = 5$–20 and radiating close to the Eddington limit. An enhancement in the intensities of various ^{12}CO transitions up the rotational ladder, as well as other molecular and atomic lines such as ^{13}CO, HCN, HCO^+, [C I], [C II], [O I], and [N II], is also expected to be observed when X-ray irradiation dominates the local gas chemistry (Meijerink et al. 2007; Spaans & Meijerink 2008). Simulations of quasars at $z \sim 6$ with massive (10^{12}–$10^{13}\ M_\odot$) halos and different merging histories showed that mid-J ^{12}CO lines are highly excited by a starburst, while high velocity peaks are expected to be produced by AGN-driven winds (Narayanan et al. 2008a, 2008b). It was further found by Narayanan et al. (2009) that the compact ^{12}CO spatial extents, broad line widths, and high excitation conditions observed in SMGs at $z \sim 2$ can be explained if SMGs are a transition phase of major merging events.

In this work, we use the XDR/PDR chemical model by Meijerink & Spaans (2005) to estimate the abundances of more than 100 species (atoms and molecules) at each grid point in the computational box of the extended 3D hydrodynamical models of an AGN torus by WPS09. We also estimate the actual X-ray flux emerging from the AGN, derived from the central black hole mass. Flux attenuation by photoabsorption of X-rays along the ray path and the distance from the central black hole is included. Thus, we estimate nonhomogeneous abundances at each grid point that depend on the local density and impinging X-ray flux. An extended version of the non-LTE 3D radiative transfer code β3D by Poelman & Spaans (2005) is used to compute the level populations of any molecule or atom for which collision data exist in the LAMDA[6] database (Schöier et al. 2005). Molecular and atomic line intensities and profiles are calculated with a line tracing approach for an arbitrary viewing angle. Model predictions for future ALMA observations of CO lines and the [C II] 158 μm fine structure line are presented. The organization of this article is as follows. In Section 2, we describe the numerical method. The results and analysis are presented in Section 3. The final remarks are presented in Section 4.

2. NUMERICAL METHOD

The 3D hydrodynamic model of the AGN torus used in this work includes inhomogeneous density fields and mechanical heating effects due to turbulence and SN explosions with a resolution (pixel size) of 0.25 pc in diameter. Detailed descriptions of the hydrodynamic equations and simulations can be found in WPS09. The 3D hydrodynamic model considers the formation and destruction of H_2 in a self-consistent way, including formation of H_2 on grains, and the destruction of it by FUV radiation. This allows the code to compute the total density, local temperature (and velocity field), as well as the fraction of H_2 at each grid element. The hydrodynamical code runs for an equivalent time of $\gtrsim$3.5 Myr until it reaches a quasi-steady state (WN02), and the gas forms a highly inhomogeneous and clumpy torus with some spiral structures. It is comprised of a flared disk of H_2 gas $\sim$50 pc in diameter, and about 10 pc in height (WPS09, their Figure 2(c)).

One of the main criticism that hydrodynamical models receive, in general, is that the density (and temperature) distribution that they show does not mimic closely actual observations

[6] http://www.strw.leidenuniv.nl/~moldata/

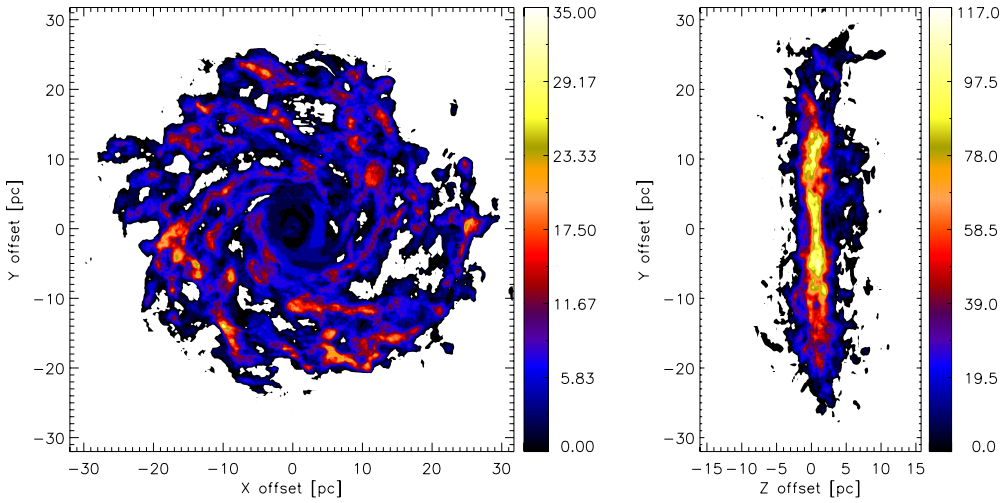

Figure 1. Number of grid elements in the 3D hydrodynamical model that has both density $n(H_2)$ higher than 10^2 cm^{-3} and temperature T_k lower than 10^4 K, along the line of sight of the *X*–*Y* plane (left) and the *Z*–*Y* plane (right). These are the grid elements that would contribute the most to the emission of molecular gas irradiated by the X-ray flux emitted from the central SMBH.

(A color version of this figure is available in the online journal.)

of the gas structure and distribution in galaxies and galaxy nuclei (like in WPS09 their Figures 2(a) and (b), their Figures 2(a) and (b))). However, observational data do not show the actual density or temperature of the gas either. The information we get from observations is the intensity and distribution of particular atomic and molecular emission (or absorption) lines, from which the ambient conditions (density, temperature, and radiation field) can be estimated. Therefore, hydrodynamical models need to be complemented with atomic and gas chemistry that allow us to infer how the emission of different species would look like given the density and temperature structure obtained from the hydrodynamic simulations.

One aspect that needs to be kept in mind is that not all the grid elements shown in density and temperature distribution maps of the 3D code by WPS09 will contribute to the emission of, particularly, molecular lines. Figure 1 shows the number of grid elements with relatively cold temperature ($T_K < 10^4$ K) and moderate density ($n(H_2) > 10^2$ cm^{-3}) that can contribute to the molecular emission emerging along the line of sight of the face-on (*X*–*Y* plane) and edge-on (*Z*–*Y* plane) viewing angles. At higher temperatures and lower densities, the fractional abundances of molecular species would be very low ($<10^{-10}$) and their contribution to the molecular emission lines would be negligible due to the low collisional excitation. The structure observed then is quite different from when we consider the full density and temperature distribution at any cross section of the computational box. Although the maps of the main contributing grid elements represent a close estimate of the structure that we would expect to observe in molecular emission, they do not take into account either the optical depth effects or the (sub-)thermal excitation of the molecular energy levels that are treated in the radiative transfer calculations described in Section 2.3. The actual structure of emission lines then depends on the local density, temperature, and the radiation flux impinging at each grid element.

The heating of the gas and dust by X-rays emanating from the AGN, as well as the chemical abundances in the cold (<500 K) gas, is not computed in hydrodynamical models. Including the (time dependent) chemical evolution at each step in the hydrodynamical simulations would take too long with the current computational resources. Therefore, after a realization of the state-of-art 3D hydrodynamical simulation, the XDR/PDR code by Meijerink & Spaans (2005) is used to estimate the chemical abundances, based on the local density and impinging X-ray flux at each grid cell of the computational box. This code is depth dependent up to large columns ($N_H \sim 10^{25}$ cm^{-2}), and considers a large (over 100 species) chemical network. In the following sections, we describe the calculation of the X-ray flux and the impact that it has on the chemistry and heating of the atomic and molecular gas around the AGN.

2.1. The X-ray Flux Model

For our 3D hydrodynamical model, we have a $M_{BH} = 1.3 \times 10^7 M_\odot$ SMBH (WPS09), so we can estimate the monochromatic luminosity of the AGN model at the rest frame wavelength $\lambda = 510$ nm as follows:

$$\lambda L_\lambda(510\,\mathrm{nm}) = 10^{44} \times \left[\frac{10^{-7}}{a}\left(\frac{M_{BH}}{M_\odot}\right)\right]^{1/b} \mathrm{erg\,s^{-1}}. \quad (1)$$

With $a = 5.71^{+0.46}_{-0.37}$ and $b = 0.545 \pm 0.036$ (e.g., Kaspi et al. 2000), we have $\lambda L_\lambda(510\,\mathrm{nm}) = 6.62 \times 10^{42}\mathrm{erg\,s^{-1}}$. Using the same bolometric to monochromatic luminosity factor as in Kaspi et al. (2000), we can determine the bolometric (total radiant energy) luminosity as $L_{bol} \approx 9\lambda L_\lambda(510\,\mathrm{nm})\mathrm{erg\,s^{-1}}$.

The incident specific flux is assumed to have a spectral shape of the form

$$F_i(E) = F_0\left(\frac{E}{1\,\mathrm{keV}}\right)^\alpha \exp(-E/E_c)\,\mathrm{erg\,s^{-1}cm^{-2}eV^{-1}}, \quad (2)$$

where $E = h\nu$eV, $\alpha \approx 0.9$ is the characteristic spectral index of the power-law components of Seyfert 1 galaxies (e.g., Pounds et al. 1990; Madejski et al. 1995; Zdziarski et al. 1995), E_c is the high energy cutoff which can be $\gtrsim$100 keV, 200 keV, or 550 keV depending on the sample of AGNs (e.g., Madejski et al. 1995), and F_0 is a constant we estimate later to match the fraction of the total luminosity emitted in X-rays at the central grid point in the data cube. On the other hand, the lower energy cutoff would depend on the shielding column density seen by the X-ray flux at each grid point. Soft X-rays (photons with energy <1 keV) cannot be effectively attenuated by columns

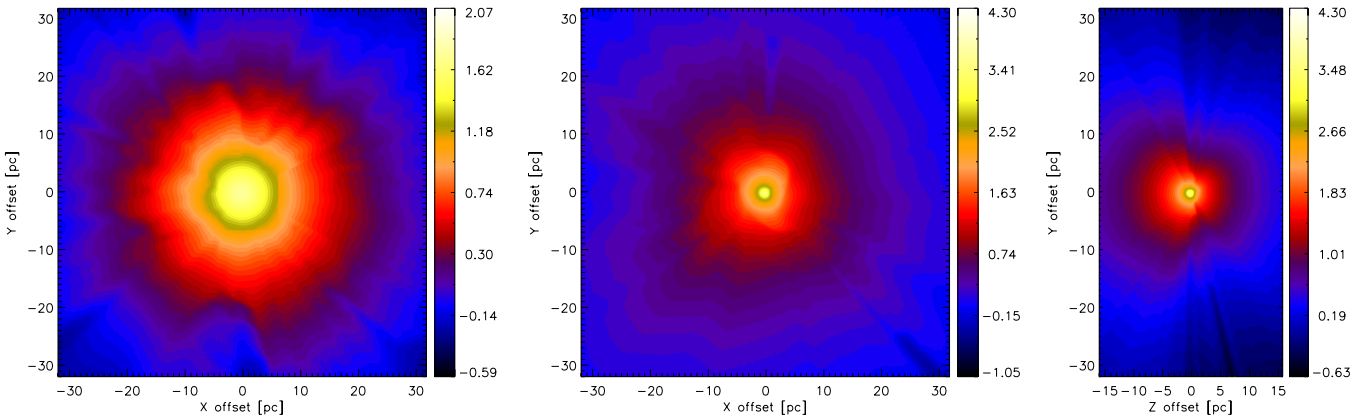

Figure 2. Impinging hard X-ray flux (in logarithmic scale and units of erg s^{-1} cm^{-2}) as seen in (left) the *X*–*Y* plane 3.5 pc below the mid-plane of the AGN torus; (middle) the flux in the actual *X*–*Y* mid-plane; and (right) the flux seen in the *Y*–*Z* plane. Note that the X-ray flux distribution is not homogeneous. The shadow-like shapes are due to the X-ray absorption by the grid cells with different densities found along the radial path from the AGN.
(A color version of this figure is available in the online journal.)

$<10^{22}$ cm^{-2}. However, as it is shown later in Section 3.1, the column densities typically found in the inner ∼25 pc of the torus are larger than 10^{22} cm^{-2}. Therefore, we only consider the hard X-rays between 1 keV and 100 keV as relevant for our X-ray chemical model. So, we integrate Equation (2) over this energy range in order to obtain the hard X-ray flux ($F_{\rm hard}$) as

$$F_{\rm hard} = \int_{1\,{\rm keV}}^{100\,{\rm keV}} F_0 \left(\frac{E}{1\,{\rm keV}}\right)^{\alpha} e^{-E/E_c} dE \,{\rm erg\,s^{-1}\,cm^{-2}}. \quad (3)$$

Considering that only ∼10% (Schleicher et al. 2010) of the total luminosity is emitted in X-rays, we have $F_{\rm hard} = 0.1 \times L_{\rm bol}/4\pi r_0^2$, where r_0 is the distance from the central black hole which, for our purpose, is assumed to be the size of a grid cell ($r_0 = \| \vec{r}_0(x_0, y_0, z_0) \| = 0.25$ pc) for the central unresolved grid point. From this we find that $F_0 \approx 1.4 \times 10^2$ erg s^{-1} cm^{-2} eV^{-1}.

For the rest of the cells, at position $\vec{r}(x, y, z)$ in the cube (a vector) the flux decreases not only with the square of the distance $r = \| \vec{r}(x, y, z) - \vec{r}_0(x_0, y_0, z_0) \|$ from the central black hole, but also because of the opacity $\tau(E, \vec{r})$ of each grid cell at position $\vec{r}(x, y, z)$ along the radial path. The opacity is defined as

$$\tau(E, \vec{r}) = \sigma_{\rm pa}(E) N_{\rm H}(\vec{r}), \quad (4)$$

where $\sigma_{\rm pa}(E)$ is the photoelectric absorption cross section per hydrogen nucleus, and $N_{\rm H}(\vec{r})$ is the total column density of hydrogen along the radial path from the central black hole to the position $\vec{r}$ in the computational box. The photoelectric absorption is calculated from all the species as

$$\sigma_{pa}(E) = \sum_i \mathcal{A}_i^{\rm total} \sigma_i(E), \quad (5)$$

with the total (gas and dust) elemental abundances, $\mathcal{A}_i^{\rm total}$, taken from Meijerink & Spaans (2005), and the X-ray absorption cross sections, $\sigma_i(E)$, from Verner & Yakovlev (1995). The total hard X-ray flux $F_{\rm hard}(\vec{r})$ (erg s^{-1} cm^{-2}) impinging on an arbitrary grid cell at position $\vec{r}$ is then calculated as

$$F_{\rm hard}(\vec{r}) = \left(\frac{0.25\,{\rm pc}}{r}\right)^2 \times \int_{1\,{\rm keV}}^{100\,{\rm keV}} F_0 \left(\frac{E}{1\,{\rm keV}}\right)^{\alpha} e^{-E/E_c} e^{-\tau(E,\vec{r})} dE. \quad (6)$$

Figure 2 shows the hard X-ray flux estimated for the 3D hydrodynamical model by WPS09 in the *X*–*Y* plane 3.5 pc below the mid-plane of the AGN torus (left panel), as well as the flux in the actual *X*–*Y* mid-plane (middle panel). The right panel shows the flux in the *Y*–*Z* plane. The grid cells with different densities cause more or less absorption of the X-ray flux along the radial path from the central SMBH, producing shadow-like shapes and an inhomogeneous flux field.

This total bolometric X-ray flux (from now on F_X) is used along with the total gas density of a grid cell as input parameters of the XDR/PDR chemistry code to estimate the abundances of several species. The formalism is described in the next section.

2.2. Chemical Abundances and Temperature

For each grid point in the computational box, we have the total gas density from the 3D hydrodynamic model. Since each grid point represents a physical (unresolved) scale of 0.25 pc, we also know the total column density that the impinging radiation flux will go through. Thus, the total gas density, the radiation flux, and the column density of each grid point are used as input parameters for the XDR/PDR chemical model by Meijerink & Spaans (2005) to compute the densities and fractional abundances of different species at different column densities throughout the 0.25 pc slab. In addition, we also get the temperature of the gas (as a function of the column density) derived self-consistently from the chemical and thermal balance computed in the XDR/PDR code. Hence, we can compare the temperatures and H_2 densities estimated from the X-ray free 3D hydrodynamical model with those computed considering the X-ray effects (see Section 3.4).

Figure 3 shows the fractional abundances of some species as a function of the column density for impinging radiation fluxes of 160 erg cm^{-2} s^{-1} (left panel) and 1.6 erg cm^{-2} s^{-1} (right panel). The slab represents a single unresolved grid point in the computational box, with a fixed scale of $d = 0.25$ pc and total hydrogen density $n_{\rm H} = 10^5$ cm^{-3}. This gives a total column density of $N_{\rm H} = n_{\rm H} \times d \approx 10^{23}$ cm^{-2}, which is marked with a vertical slashed-dotted line. The XDR/PDR model, though, was executed to compute the abundances of the species up to a column of 10^{25} cm^{-2} in order to show how deep the X-rays can penetrate depending on the strength of the radiation field. For the strong X-ray flux (left panel) and the actual column density (∼10^{23} cm^{-2}) of the slab, the abundances of molecules

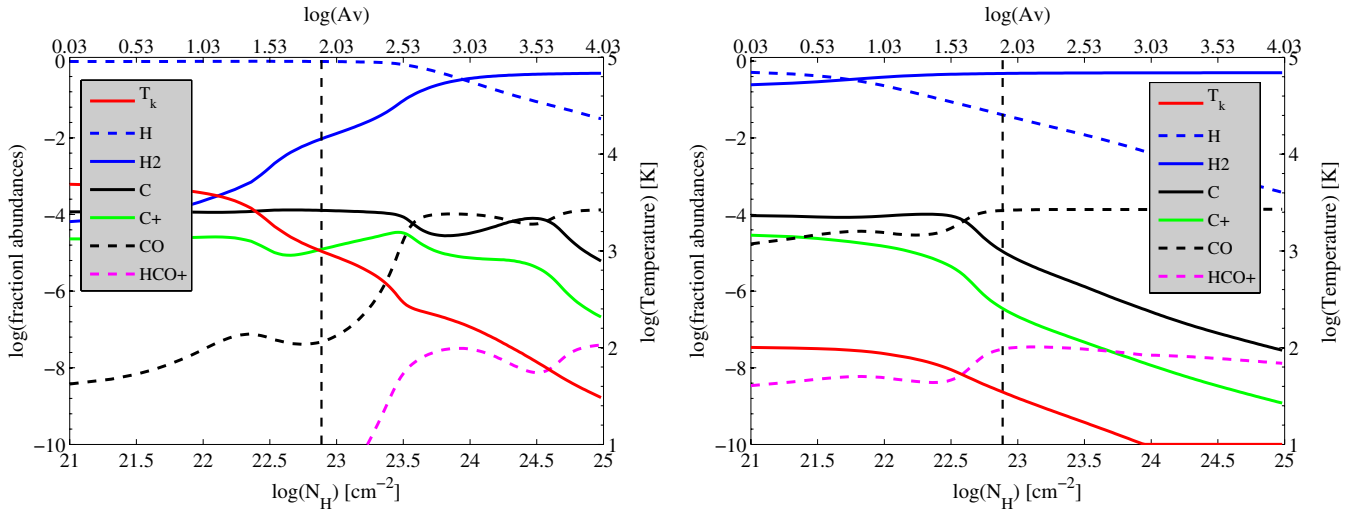

Figure 3. Left panel: fractional abundances of various atomic and molecular species in a slab that represents one unresolved grid cell of $d = 0.25$ pc and density of $n_{\rm H} = 10^5\,{\rm cm}^{-3}$ in the 3D hydrodynamic model. The X-ray flux of $160\,{\rm erg\,cm}^{-2}\,{\rm s}^{-1}$ penetrates on the left side of the slab and affects the chemistry as it is absorbed throughout the column of gas and dust. The vertical dashed-dotted line indicates the total column density $N_{\rm H} = n_{\rm H} \times d \approx 8 \times 10^{22}\,{\rm cm}^{-2}$ of the slab. For this particular X-ray flux, a denser slab would be required to observe a significant abundance of molecules like HCO^+. Right panel: fractional abundance for the same slab as above, but with an impinging radiation flux of $1.6\,{\rm erg\,cm}^{-2}\,{\rm s}^{-1}$. Note the higher abundances of H_2, CO, and HCO^+ at lower column densities, while the abundance of H, C, and C^+ decrease earlier and faster throughout the slab. The overall temperature is also lower in this case.

(A color version of this figure is available in the online journal.)

like HCO^+ will be negligible. Since the scale of the grid points is fixed, a slab denser than $10^5\,{\rm cm}^{-3}$ would be required in order to observe a significant abundance of HCO^+ at larger ($N_{\rm H} > 10^{23}\,{\rm cm}^{-2}$) columns. Conversely, a weaker radiation flux of $1.6\,{\rm erg\,cm}^{-2}\,{\rm s}^{-1}$ (right panel) impinging on the slab will produce a higher abundance of, e.g., H_2, CO, HCO^+ at lower column densities, while H, C, and C^+ would be less abundant, in a column-averaged sense, than in the previous case. An overall lower temperature is also observed when the radiation flux is weaker, since X-ray photons are completely absorbed at a column of $\gtrsim 10^{24}\,{\rm cm}^{-2}$.

Since a grid point of the 3D hydrodynamic model is unresolved and the chemical abundances given by the XDR/PDR code depend on the column density, we estimate an abundance that is *representative* for the particular slab and for each species in the chemical network from the abundances observed throughout the slab of 0.25 pc. We compute the total fractional abundance $\langle \mathcal{A}_X \rangle$ of the species $X = {}^{12}$CO, HCN, etc., as

$$\langle \mathcal{A}_X \rangle = \frac{\int n_X(l) dl}{\int n_{\rm H} dl}, \tag{7}$$

where $n_X(l)$ (${\rm cm}^{-3}$) is the density of the species X at the layer l (cm) in the cloud and $n_{\rm H}$ is the total density of the slab, so the denominator is actually the total column density $N_{\rm H}$ (${\rm cm}^{-2}$) of a particular grid point.

Because the variation of the abundance of a species through the slab is different for every species (e.g., [C I] is more abundant at the edge of the slab where T is high, while ^{12}CO is more abundant deep into the slab, where T is low), we require a gas temperature that is representative of the layers in the slab where the abundance of the species is higher (since those layers contribute the most to the line emission). Therefore, we compute an abundance-weighted average temperature, throughout an unresolved grid point, as

$$\langle T_X \rangle = \frac{\int \mathcal{A}_X(l) T(l) dl}{\int \mathcal{A}_X(l) dl}, \tag{8}$$

which gives different temperatures for different species in the same grid point. For instance, with the lower ($1.6\,{\rm erg\,cm}^{-2}\,{\rm s}^{-1}$) X-ray flux (right panel in Figure 3), the total fractional abundance of CO is $\sim 10^{-4}$ with an abundance-weighted average temperature of ~ 37 K, while for C we have an abundance of $\sim 3 \times 10^{-5}$ and a representative temperature of ~ 66 K.

Due to the large number of grid elements in the hydrodynamical model ($256 \times 256 \times 128 \sim 8.4 \times 10^6$ data points), we require an optimized process in order to run the XDR/PDR code for the essential grid elements. Our criterion was to process only the grid points with total density larger than $100\,{\rm cm}^{-3}$ and temperature lower than 10^4 K. This is because lower gas densities will have little weight in the excitation of the molecular species, while higher temperatures would lead to mostly ionized gas. Once the abundances and abundance-weighted average temperatures have been determined for the selected grid elements of the 3D hydrodynamical model, we can proceed to perform the radiative transfer calculations for the entire cube.

2.3. 3D Radiative Transfer and Line Tracing

The advanced 3D radiative transfer code β3D (Poelman & Spaans 2005) has been optimized for heavy memory usage to be able to use the $256 \times 256 \times 128$ element data cube of the low-resolution (0.25 pc scale) 3D hydrodynamical models by WPS09. In principle, the temperature, density, and velocity field derived from the hydrodynamical simulations can be used as the ambient conditions for the radiative transfer formalism. However, the temperature derived from the XDR model is found to be significantly different from the temperature obtained in the hydrodynamical model, as discussed in Section 3.4. A multi-zone radiative transfer approach is used in which the calculation of the level populations in a grid cell depends on the level populations of all the other cells through the different escape probabilities connecting adjacent grid points (Poelman & Spaans 2005, 2006).

The collisional rates available in the LAMDA database (Schöier et al. 2005) are used in a way similar to the

one-dimensional (1D) and two-dimensional (2D) radiative transfer codes RADEX (van der Tak et al. 2007) and RATRAN (Hogerheijde & van der Tak 2000) to calculate the level populations of different atomic and molecular species (e.g., [C I], [C II], [O I], ^{12}CO, ^{13}CO, HCN, HCO$^+$, HNC, CN, etc.). For this we use the commonly adopted main collision partner H_2 for the radiative transfer calculations of all the molecules. Although the contribution of helium atoms to the total collision density for CO is just about 10^{-2}, we also include (for completeness) He as an additional collision partner by extrapolating (see Appendix A) the rate coefficients reported in Cecchi-Pestellini et al. (2002). For the case of [C II] discussed in Section 3.3, we also use H and electrons as collision partners. With the exception of electrons, the density of all the collision partners n(H) and $n(H_2)$ at each grid point is given by the hydrodynamical model (as described in WPS09), since our aim is to know how the line emissions would look like for this particular model of an AGN torus. The hydrodynamical model, however, does not yet trace the evolution of electron density. So, we use $n(e^-)$ derived from the XDR model.

The line intensities, including kinematic structures in the gas, and optical depth effects are computed with a ray-tracing approach for arbitrary rotation (viewing) angles about any of the three axes of the computational box. The emerging specific intensity is computed using the escape probability formalism described in Poelman & Spaans (2005),

$$dI_\nu^z = \frac{1}{4\pi} n_i A_{ij} h\nu_{ij} \beta(\tau_{ij}) \left(\frac{S_{ij} - I_b^{\rm loc}(\nu_{ij})}{S_{ij}} \right) \phi(\nu_{ij}) dz, \qquad (9)$$

where dI_ν^z has units of erg cm^{-2} s^{-1} sr^{-1} Hz^{-1}, n_i is the population density in the ith level, A_{ij} is the Einstein A coefficient, $h\nu_{ij}$ is the energy difference between the levels i and j, S_{ij} is the source function for the corresponding transition, $I_b^{\rm loc}(\nu_{ij})$ is the local background radiation at the frequency of the transition, and τ_{ij} is the *cumulative optical depth* that increases away from the observer from the edge of the ray path to the zth layer.

3. ANALYSIS AND RESULTS

Once the level populations of particular transitions have been estimated with the radiative transfer code and the line tracing at a particular inclination angle has been completed, the resulting 2D emission map can be exported into a regular FITS data cube.

3.1. CO Maps

The total hydrogen column density $N_{\rm H}$, for a face-on viewing angle of the 3D hydrodynamical model, is shown in the top left panel of Figure 4. As expected, the total column density of the CO molecule N(CO) (top right panel) follows a similar distribution, although with about four orders of magnitude lower columns. The left and right bottom panels of Figure 4 show the surface brightness of the CO $J = 1 \rightarrow 0$ and $J = 6 \rightarrow 5$ lines, respectively. These correspond to the brightness observed at the surface of the face-on data cube (i.e., not scaled for an arbitrary distance to the source). Given the relatively lower upper energy state (∼5.53 K) and critical density (∼2×10^3 cm^{-3} at 100 K) of the CO $J = 1 \rightarrow 0$ line, most of the warm and dense gas and structure is traced by the CO $J = 6 \rightarrow 5$ line instead. The emission of the lower CO $J = 1 \rightarrow 0$, $J = 2 \rightarrow 1$, and $J = 3 \rightarrow 2$ transitions trace with relatively fainter emission (or not trace at all) the inner region of the torus, while the higher CO lines (from $J = 4 \rightarrow 3$ up to $J = 9 \rightarrow 8$) strongly trace the inner structures, including the inner narrow-line region (NLR) of the torus. This is also shown by the CO 3–2/1–0 and 6–5/1–0 line intensity ratios of Figure 5 (top panels). This can be explained by an optically thick $J = 1 \rightarrow 0$ line (N(CO) $> 10^{18}$ cm^{-2}) and by the modest presence of cold (<100 K) gas, specially at the inner ±5 pc of the AGN torus. This indicates that, by just considering the excitation of CO, the $J = 1 \rightarrow 0$ line will not always be a good tracer of hydrogen column density $n_{\rm H}$ in the central region ($\lesssim$60 pc) of an AGN. The same can be concluded from the emission maps obtained considering an inclination angle of 45° about the X-axis. This is shown in Figure 12 of Appendix B.

As an exercise for comparison with future observations, we simulate a raster map of the AGN torus by adopting a distance $D = 3.82$ Mpc (the distance to NGC 4945) to the source and by convolving the surface brightness maps with a single dish beam of FWHM = 0.″15 (about 11 pixels in the original map). This corresponds to a spatial scale of ∼2.8 pc at the distance chosen and gives a flux with units of 10^{-15} erg s^{-1} cm^{-2} after multiplying the surface brightness by the solid angle $d\Omega = dR^2/D^2$ subtended by the original pixel scale ($dR = 0.25$ pc) at the adopted distance of the source. A step size of one-third the FWHM (∼0.92 pc, or about 4 pixels) degrades the original image from 256 × 256 to a 61 × 61 pixels image. Figure 5 (bottom panels) shows the resulting flux maps of the CO $J = 1 \rightarrow 0$ (left) and CO $J = 6 \rightarrow 5$ (right) lines. All the set of transitions from $J = 1 \rightarrow 0$ to $J = 9 \rightarrow 8$ is shown in Figure 13 of Appendix B. The smearing effect of the relatively large beam produces the loss of the intricate structure observed in the original maps with 0.25 pc resolution shown in Figure 4, while a torus-like shape becomes more evident in the CO $J = 1 \rightarrow 0$ line.

3.2. The Relation between CO and Gas Mass

In the last few decades, the integrated line fluxes of the lower ^{12}CO rotational lines (1–0, 2–1, and 3–2) have been used to estimate the gas masses of molecular clouds in the Milky Way (e.g., Dickman et al. 1986; Solomon et al. 1987; Solomon & Barrett 1991, and references therein). These estimates hold for the Milky Way and nearby normal galaxies, where the CO emission emerges from moderately dense (volume-averaged densities of $n(H_2) \sim 500$ cm^{-3}) giant molecular clouds in virial equilibrium (i.e., self-gravitating). For spherical clouds supported by isotropic random motions (e.g., turbulence) in virial equilibrium, the resulting inferred theoretical conversion factors are $X \sim 2 \times 10^{20}$[cm^{-2}(K km s^{-1})$^{-1}$] and $\alpha = 4.3[M_\odot$(K km s^{-1})$^{-1}$] (Strong & Mattox 1996; Dame et al. 2001; Dickman et al. 1986; Solomon et al. 1987).

The virial approach of the optically thick CO lines can be extended to other galaxies, considering an ensemble of virialized clouds, instead of a single one (Dickman et al. 1986). In galactic nuclei and starburst galaxies, however, the assumption of an ensemble of individual gas clouds in virial equilibrium does not hold. In these environments the gas motions are due to a combination of gas and stellar mass components, and the gas is expected to be in a smoother configuration along a disk. Nevertheless, Downes et al. (1993), Solomon et al. (1997), and Downes & Solomon (1998) have shown that a slightly modified version of the CO luminosity to gas mass conversion factors can be derived in these environments. For luminous or ultraluminous infrared galaxies, the inferred theoretical conversion factors range between $\alpha = 0.8$ and 1.6, or $X = (3.7–7.3) \times 10^{19}$ (Solomon et al. 1997; Downes & Solomon 1998).

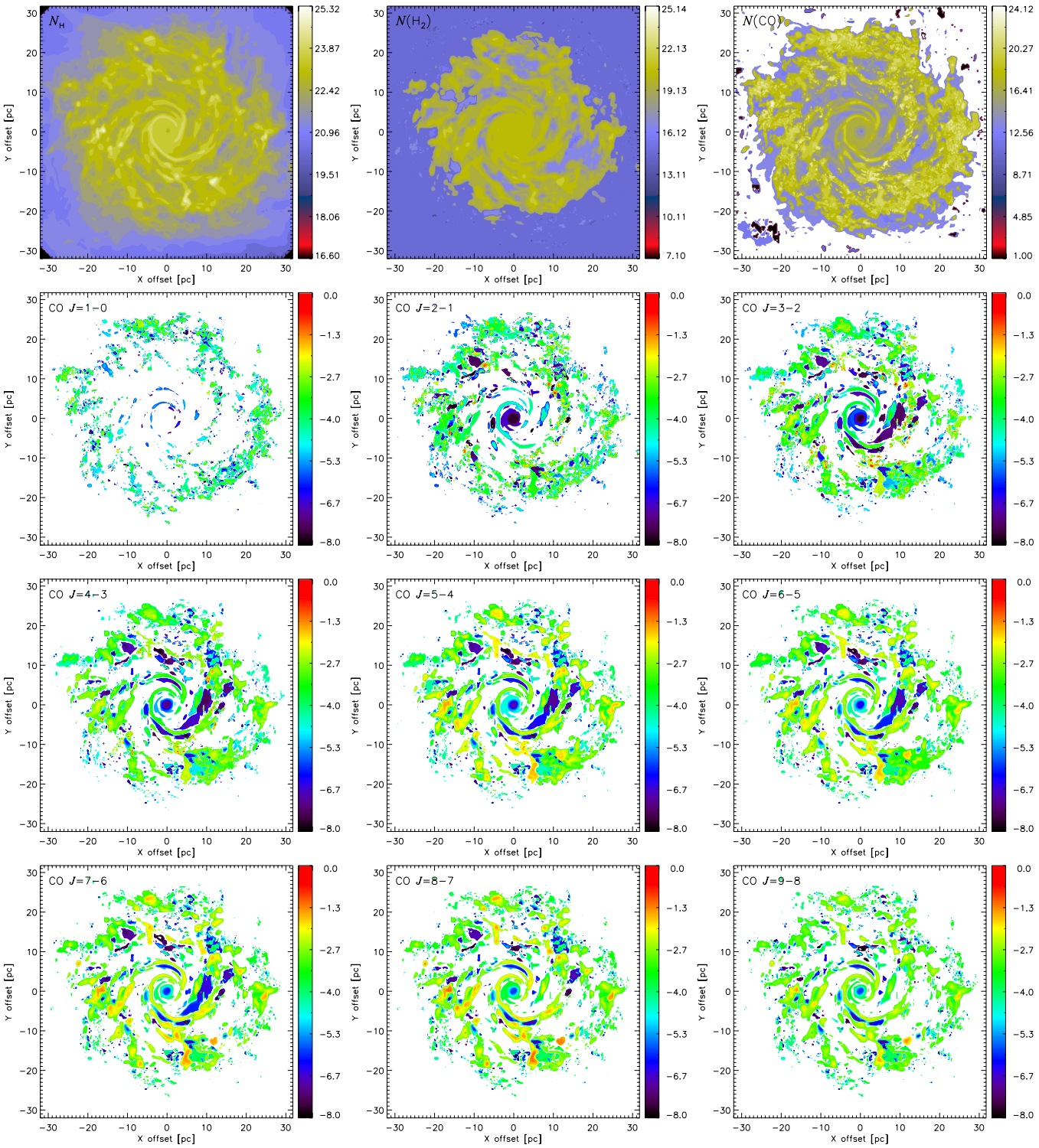

Figure 4. Top panels: face-on view of the total column density (units of cm^{-2}) N_{H} (left), the column density of molecular hydrogen $N(\mathrm{H}_2)$ (middle) and CO column $N(\mathrm{CO})$ (right) in logarithmic scale. Bottom panels: surface brightness maps of the $J = 1 \rightarrow 0$ to $J = 9 \rightarrow 8$ transitions of CO (in $\log_{10}$ scale and units of $\mathrm{erg\,s^{-1}\,cm^{-2}\,sr^{-1}}$), as observed at the surface of the face-on data cube. The emission of the lower CO $J = 1 \rightarrow 0$, $J = 2 \rightarrow 1$, and $J = 3 \rightarrow 2$ transitions do not trace (or just with relatively fainter emission) the inner region of the torus, while the higher CO lines (from $J = 4 \rightarrow 3$ up to $J = 9 \rightarrow 8$) do trace the inner spiral structures, including the inner NLR.

(A color version of this figure is available in the online journal.)

Since we know exactly what the gas mass in our models is, we can explore the behavior of the CO-to-H_2 conversion factor in our model of an AGN torus from the computed luminosities of several CO rotational lines. First, we check the relation between the *average* density $\langle n_{\mathrm{H}} \rangle$ and the *average* abundance-weighted temperature of CO $\langle T_{\mathrm{CO}} \rangle$ (computed through the line of sight or column) for each pixel of the map at the original resolution. We apply a similar criteria as in Section 2.2 when computing the average density and temperature. That is, we use only the grid points with total densities n_{H} larger than $100\,\mathrm{cm}^{-3}$ and

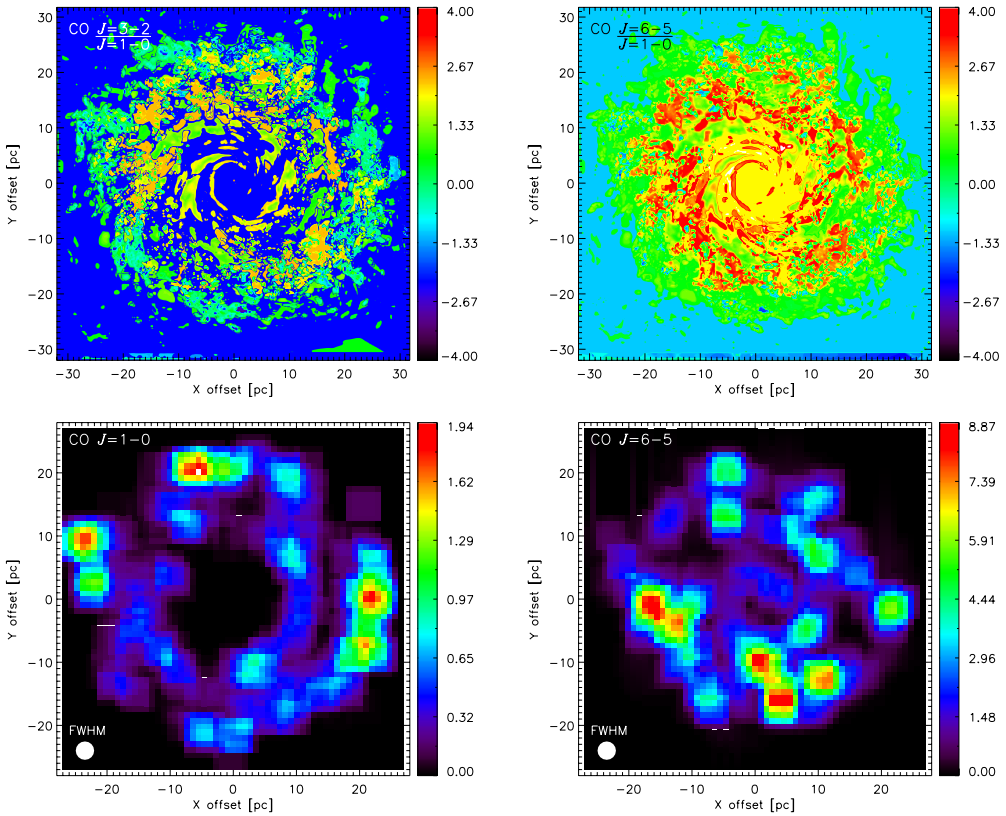

Figure 5. Top panels: maps of the CO 3–2/1–0 (left) and CO 6–5/1–0 (right) line intensity ratios. Bottom panels: face-on view of the flux (10^{-15} erg s^{-1} cm^{-2}) of the CO $J = 1 \rightarrow 0$ (left) and CO $J = 6 \rightarrow 5$ (right) lines, as mapped with a single dish beam of FWHM = 0.″15 (∼2.8pc) and adopting a distance $D = 3.82$ Mpc to the source. Note how the relatively large beam smears out the intricate structure observed in the maps with the original resolution (0.25 pc) shown in Figure 4. These lower resolution maps make more evident the fact that the $J = 1 \rightarrow 0$ line traces the more diffuse outer gas, while the $J = 6 \rightarrow 5$ traces the denser gas of the inner NLR.

(A color version of this figure is available in the online journal.)

temperatures $T_{\rm CO}$ lower than 5000 K to compute $\langle n_{\rm H} \rangle$ and $\langle T_{\rm CO} \rangle$. This criterion, however, produces several pixels with $\langle n_{\rm H} \rangle = 0$, specially in the outer region of the maps. Then we generate lower resolution raster maps by convolving the original resolution (0.25 pc) maps of $\langle n_{\rm H} \rangle$ and $\langle T_{\rm CO} \rangle$ with different beam sizes (FWHM) corresponding to 1.75 pc, 4.75 pc, and 9.25 pc (with step or pixel sizes of ∼FHWM/3), as it was done in Section 3.1. Those pixels with $\langle n_{\rm H} \rangle = 0$ are masked out in both density and temperature maps during the convolution process. From all the pixels of the raster maps, we create scatter plots of $\langle n_{\rm H} \rangle$ versus $\langle T_{\rm CO} \rangle$ at the different resolutions.

The density and temperature maps, as well as the corresponding scatter plots, are shown in Figure 6. The $\langle n_{\rm H} \rangle$ and $\langle T_{\rm CO} \rangle$ maps (first and second column in Figure 6, respectively) show denser and colder gas in the center of the AGN torus, indicating an *inverse* relation between the average density and temperature (i.e., higher densities correspond to lower temperatures). The third column in Figure 6 shows the scatter plots obtained considering all the pixels in the maps, where the expected *inverse* relation between $\langle n_{\rm H} \rangle$ and $\langle T_{\rm CO} \rangle$ is reproduced at all the resolutions. The relation between density and temperature becomes tighter and almost linear in the maps convolved with larger beams.

Similarly, for each pixel of the CO maps we compute the total gas mass $M_{\rm gas}$ by adding the individual masses of each grid point along the line of sight, and the CO luminosity $L'_{\rm CO}$ derived from the CO intensity maps obtained in Section 3.1. In this case, we do not apply the criteria $n_{\rm H} > 100\,{\rm cm}^{-3}$ and $T_{\rm CO} < 5000$ K as before in order to obtain the actual total $M_{\rm gas}$ of the hydrodynamical model along the line of sight. However, we use the previously obtained average density map in order to mask the pixels with $\langle n_{\rm H} \rangle = 0$ in the gas mass and CO luminosity maps as well. This is because those pixels correspond to CO emission that is more than five orders of magnitude lower than the peak CO emission produced from our model. Given that is unlikely to have such large dynamical range in a real detector, the lower emission would be even below the noise level that could be found in maps obtained from real observations. Thus, not masking these pixels would cause an artificial bias toward lower luminosities during the convolution process. An alternative approach to masking pixels is to add random background noise to our intensity maps. However, the noise level to be added is arbitrary, so the results can be made at least comparable, and we are actually more interested in showing what is really coming out from the hydrodynamical and XDR models.

Figure 7 shows the scatter plots of the gas masses ($M_{\rm gas}$) and the CO luminosity ($L'_{\rm CO}$ [K km s^{-1} pc^2]) of the $J = 1 \rightarrow 0$, $J = 6 \rightarrow 5$, and $J = 9 \rightarrow 8$ transitions as obtained from the low-resolution (0.25 pc) hydrodynamical model. We consider a 36% mass correction to account for the mass of helium atoms. The straight line corresponds to the gas mass estimated assuming a luminosity-to-gas mass conversion factor α of $M_{\rm gas}/L'_{\rm CO} = \alpha = 0.8$ (e.g., Solomon et al. 1997; Downes & Solomon 1998). The result of the original resolution shows a

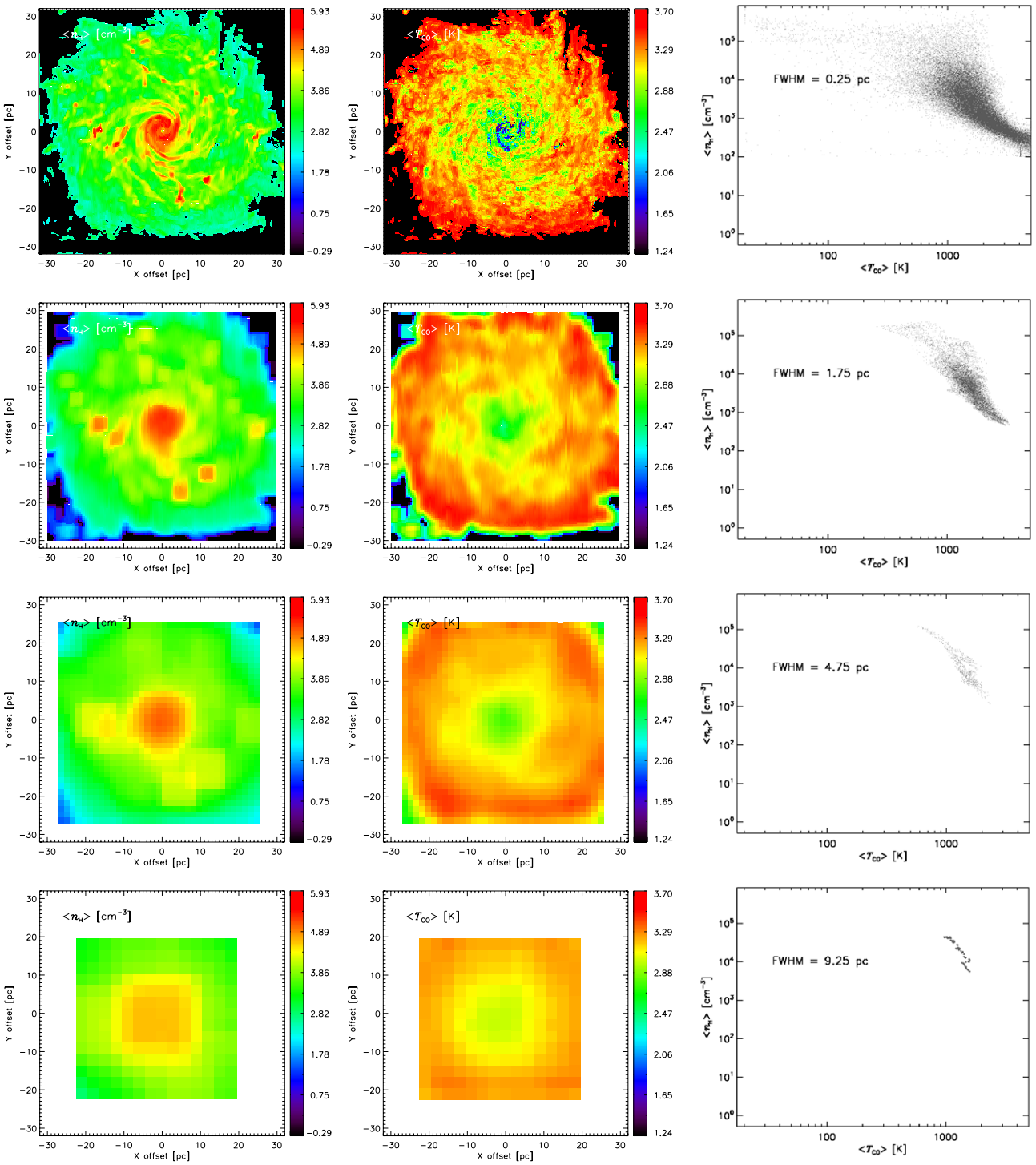

Figure 6. Two-dimensional maps (at the original resolution of 0.25 pc) of the average density $\langle n_{\rm H} \rangle$ (left panels), the average abundance-weighted temperature $\langle T_{\rm CO} \rangle$ of CO (middle panels), and scatter plot of $\langle n_{\rm H} \rangle$ vs. $\langle T_{\rm CO} \rangle$. From top to bottom: same as in the top panels but convolving the maps with beam sizes (FWHM) equivalent to 1.75 pc, 4.75 pc, and 9.25 pc, for a distance of 3.82 Mpc to the source. For the lowest resolution maps the scatter plot is shown with larger symbols for better visualization. All the scatter plots show the expected inverse relation between $\langle n_{\rm H} \rangle$ and $\langle T_{\rm CO} \rangle$: lower temperatures correspond to higher densities, and they converge to a linear relation as the beam size increases.

(A color version of this figure is available in the online journal.)

large scatter of gas masses for a given CO luminosity. When considering the source at a nominal distance of 3.82 Mpc, however, the beam-averaged masses and luminosities result in a tighter correlation, but still with a considerable scatter. The relation between $L'_{\rm CO}$ and $M_{\rm gas}$ is clustered just at the higher luminosity and mass ranges as the beam size increases. That is, the pixels with lower mass and luminosity are missing (beam smeared) in the lower resolution maps. The higher the CO J line and the larger the beam used, the closer is the relation found with our models to the luminosity-to-gas mass conversion factor proposed in the literature. The α factor was estimated based on the lower transitions ($J = 1 \rightarrow 0$, $J = 2 \rightarrow 1$, and

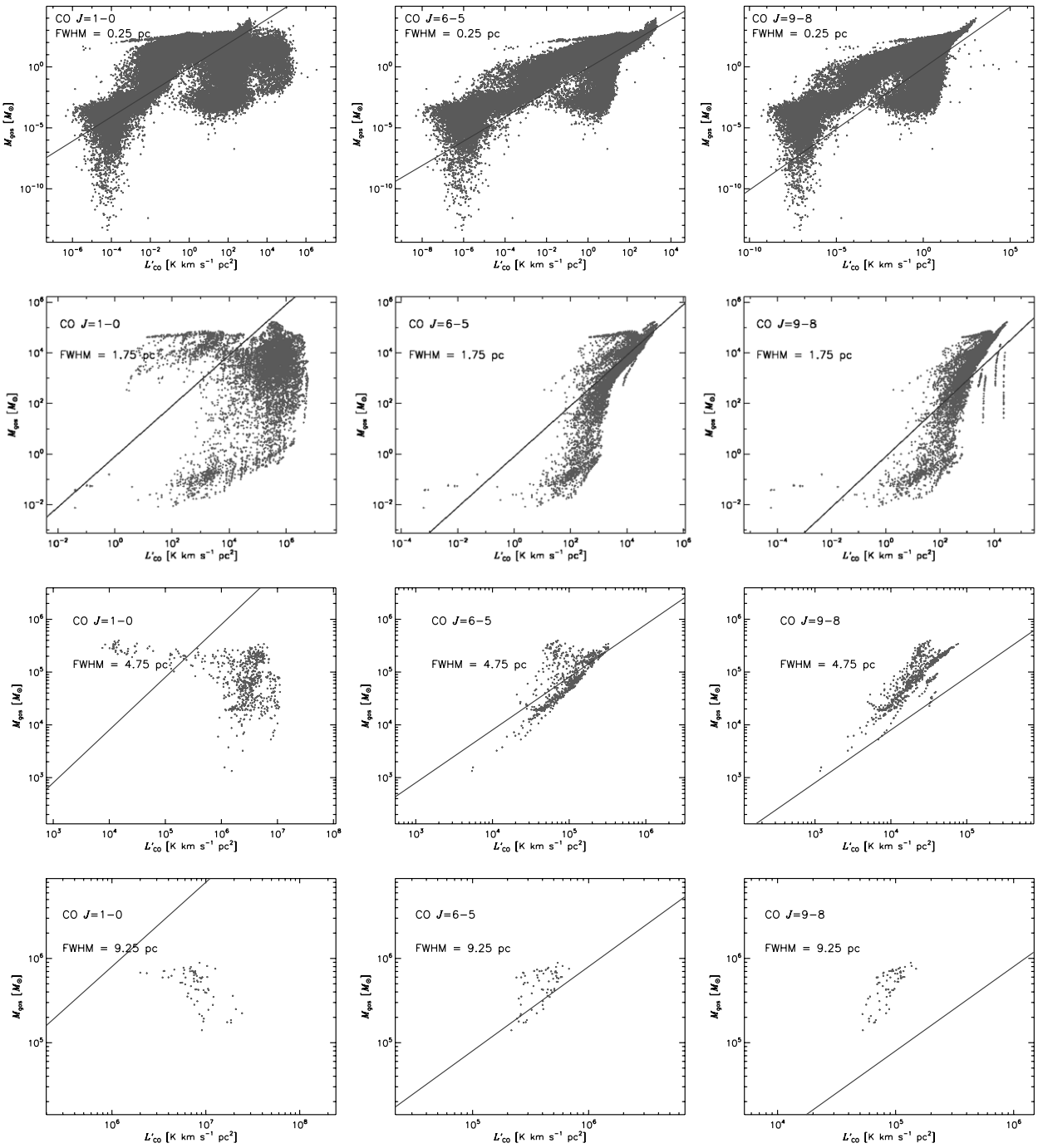

Figure 7. Scatter plots between the ensemble of gas masses ($M_{\rm gas}$ [$M_\odot$]) and the CO luminosity ($L'_{\rm CO}$ [K km s^{-1} pc^2]) of the (from left to right) $J = 1 \rightarrow 0$, $J = 6 \rightarrow 5$, and $J = 9 \rightarrow 8$ transitions derived from the low resolution (0.25 pc) hydrodynamical model, and convolved (beam averaged) with beam sizes (FWHM) equivalent to 0.25 pc (the original scale of the model), 1.75 pc, 4.75 pc, and 9.25 pc (from top to bottom, respectively), for a distance of 3.82 Mpc to the source. The straight line corresponds to the gas mass estimated assuming a luminosity-to-gas mass conversion factor α of $M_{\rm gas}/L'_{\rm CO} = \alpha = 0.8$ (e.g., Solomon et al. 1997; Downes & Solomon 1998). The gas mass used here includes a 36% correction to account for helium. Note the different scales of the axes for different resolutions and J-lines.

$J = 3 \rightarrow 2$), which are way off in our models because there is very little cold ($T_{\rm CO} < 100$ K) gas in the inner 60 pc. Besides, the relatively large scatter observed at all resolutions indicates that many of the clumps where the CO emission emerges from are not in virial equilibrium. On the other hand, the CO $J = 6 \rightarrow 5$ and $J = 9 \rightarrow 8$ transitions show similar trends. This implies that the higher J line does not provide significant additional information compared to the $J = 6 \rightarrow 5$ line.

We can confirm then a tight correlation between the beam-averaged luminosity of the higher CO J lines (from $J = 5 \rightarrow 4$ to $J = 9 \rightarrow 8$) and the gas mass of the AGN torus. However, the larger scatter seen when using higher resolution (smaller beam sizes) should be taken as a warning sign for future higher resolution observations like ALMA, which may no longer show a linear correlation between CO luminosity and gas mass, or may introduce a larger range of correlations for ensembles of clouds with different density and high temperature structures. So, using only mid-J CO lines (like $J = 6 \rightarrow 5$) for gas mass determinations in AGN tori would be the most reliable approach.

3.3. The [C II] 158 μm Fine Structure Line

A considerable amount of gas close to the SMBH is predicted to be at very high temperatures ($T_k > 1000$ K) in the 3D hydrodynamical model. At these temperatures hydrogen is found mostly in atomic form, and other atoms like carbon are mostly ionized. Therefore, in this section we present the results of the radiative transfer calculations done for [C II]. We use the collision rate coefficients of [C II] from the LAMDA database. In contrast with the CO molecule, we considered not only the molecular hydrogen as a collision partner but also the atomic hydrogen and the electrons, using the collision data reported by Flower & Launay (1977), Launay & Roueff (1977), and Wilson & Bell (2002). These are the most relevant collision partners for [C II] in an AGN environment, since their densities are expected to be higher than $n(H_2)$ in the very hot gas ($T_k > 1000$ K) regions. As described in Sections 2.2 and 2.3, the fractional abundance of the electrons is derived from the XDR model, while the density n(H) is computed from the hydrodynamical model as $n(H) = n_H - 2n(H_2)$ (Wada et al. 2009).

Figure 8 shows the face-on view (left panels) of the total column density $N(e^-)$ (cm^{-2}) of electrons, the surface brightness (in $\log_{10}$ scale and units of $\mathrm{erg\,s^{-1}\,cm^{-2}\,sr^{-1}}$) of the [C II] 158 μm emission at the original spatial resolution (0.25 pc), and at $\sim$ 2.8 pc resolution (for a distance $D = 3.82$ Mpc to the source) after convolving the original map with a single dish beam of FWHM = 0.″15. This results in a flux with units of $10^{-15}\mathrm{erg\,s^{-1}\,cm^{-2}}$ after multiplying the surface brightness by the solid angle as described in Section 3.1. Comparing with the CO emission shown in Figures 4 and 5, it is clear that the [C II] 158 μm emission traces mostly the central region (inner NLR) of the AGN torus, and it is a better tracer of the hot regions than the mid-J CO lines.

The right panels of Figure 8 show the same as in the left panels, but with an inclination angle of 45° about the X-axis. The viewing angle produces a slightly larger column of [C II] observed through the line of sight, which in turn results in a ∼30% brighter [C II] 158 μm peak emission. The [C II] 158 μm emission (rest frequency ∼1900 GHz) from galaxies at redshift $z \gtrsim 1$ will be observable with ALMA. Unfortunately, we cannot obtain high-resolution maps of [C II] with the current specifications of ALMA. Even if we consider both the largest baseline of 16 km and the highest frequency of 950 GHz (band 10) that ALMA is expected to have in the future, we could get a resolution of FWHM[7] ∼ 60/16(km)/950(GHz) ∼ 0.″004. This in turn gives a spatial scale of 32 pc for a source at $z = 1$ (with an equivalent angular distance of 1658.6 Mpc, in a ΛCDM cosmology with $H_0 = 71$ km s^{-1} Mpc^{-1}). That is, the whole region we show in Figure 8 would correspond to just one or two pixels in the ALMA maps of sources at $z = 1$.

3.4. Temperature and Density Driven by X-rays

In Equation (6), we assumed that the X-ray flux is spherically symmetric with respect to the central SMBH. If we assume instead that the X-rays are emitted in a preferential direction perpendicular to the mid-XY-plane of the accretion disk (and of the AGN torus as a whole), we can consider the X-ray flux emerging from a Lambertian object. That is, the radiation flux impinging on each grid point of the cube is proportional to the cosine of the viewing angle θ with respect to the vertical Z-axis. This means that the X-ray flux would be negligible in the disk (mid-plane) of the AGN torus.

[7] http://science.nrao.edu/alma/specifications.shtml

In order to compare the impact that the two different X-ray flux distributions have on the temperature and molecular hydrogen density of the gas, we compare the temperature T_{HYD} obtained from the hydrodynamical model with the H_2 abundance-weighted average temperature T_{XDR} (Equation (8)) derived from the XDR chemical model using both the *spherical* and *Lambertian* X-ray fluxes. We take a strip volume of $64 \times 1.25 \times 1.5\,\mathrm{pc}^3$ along the X-axis, and around the center of the Y-axis ($\Delta Y = 0$) and Z-axis ($\Delta Z = 0$) of the 3D cube. We use this *thin* volume so we can have similar X-ray fluxes (decreasing mostly with radial distance) impinging at each grid element of the $1.25 \times 1.5\,\mathrm{pc}^2$ slices of the volume. We computed the average temperature and H_2 density of the $1.25 \times 1.5\,\mathrm{pc}^2$ slices at each ΔX grid element. At the resolution of 0.25 pc/element we have 30 grid elements per slice, which is a good compromise between a representative number of grid elements and a fairly constant impinging X-ray flux at each slice.

The top panel of Figure 9 shows the average temperature T_{HYD} (K) estimated in the 3D hydrodynamical model (solid line) at each ΔX grid element. The corresponding average (of the H_2 abundance-weighted average) temperature T_{XDR} (K) obtained from the XDR chemical model is shown with a gray line. Only the grid elements with $T_{HYD} < 10^4$ K were used in the XDR model, and they are shown with filled circles. The average T_{XDR}/T_{HYD} ratio (gray line + filled circles) and the average X-ray flux (solid black line) F_X ($\mathrm{erg\,s^{-1}\,cm^{-2}}$) are shown in the bottom panel of Figure 9. The average relative temperature is directly related to the impinging flux at each ΔX grid element, and decreases as the X-ray flux decreases. The temperature derived from the XDR model is higher ($T_{XDR}/T_{HYD} > 1$) than the one estimated in the hydrodynamical model. Hence, the presence of X-rays has an undeniable effect on the thermodynamics of the AGN torus, up to at least 60 pc.

In Figure 10, the average density of molecular hydrogen $n(H_2)_{HYD}$ along a $64 \times 1.25 \times 1.5\,\mathrm{pc}^3$ strip volume is shown. The density computed for the 3D hydrodynamical model is shown by the solid line, and the corresponding average $n(H_2)_{XDR}$ density obtained from the XDR chemical model, using the *spherical* (top panels) and the *Lambertian* (bottom panels) X-ray fluxes, is shown with the gray line + filled circles. Only the data points for grid cells with $T_{HYD} < 10^4$K and $n(H_2)_{HYD} > 10^{-2}\,\mathrm{cm}^{-3}$ are shown in the figure.

The relative H_2 density seems to be inversely related to the impinging flux. That is, the average $n(H_2)_{XDR}$ density derived from the XDR model is lower (by factors up to ∼10^4) than the average H_2 density of the hydrodynamical model. This is observed in the inner ±10 pc region around the center of the AGN torus. This is mostly the consequence of relatively *thin* slabs ($N_H < 10^{23}\,\mathrm{cm}^{-2}$) being irradiated by a rather strong ($F_X > 1.6\,\mathrm{erg\,s^{-1}\,cm^{-2}}$) X-ray flux in the proximity of the torus center, as described in Section 2.2 and shown in Figure 3. However, beyond $\Delta X \sim 10$ pc the XDR H_2 abundance exceeds the one in the pure hydrodynamical model. This change is explained by the background star formation considered in the hydrodynamical model at those distances. The FUV is a more efficient destroyer of the H_2 gas than X-rays (Meijerink & Spaans 2005).

With a *spherical* X-ray flux $n(H_2)_{XDR}$ can be up to 10^4 times higher than $n(H_2)_{HYD}$, while it can be about 10^5 higher if a *Lambertian* X-ray flux is considered instead. In the inner region ($\Delta X \sim -2$ pc), a density $n(H_2)_{XDR}$ a few times

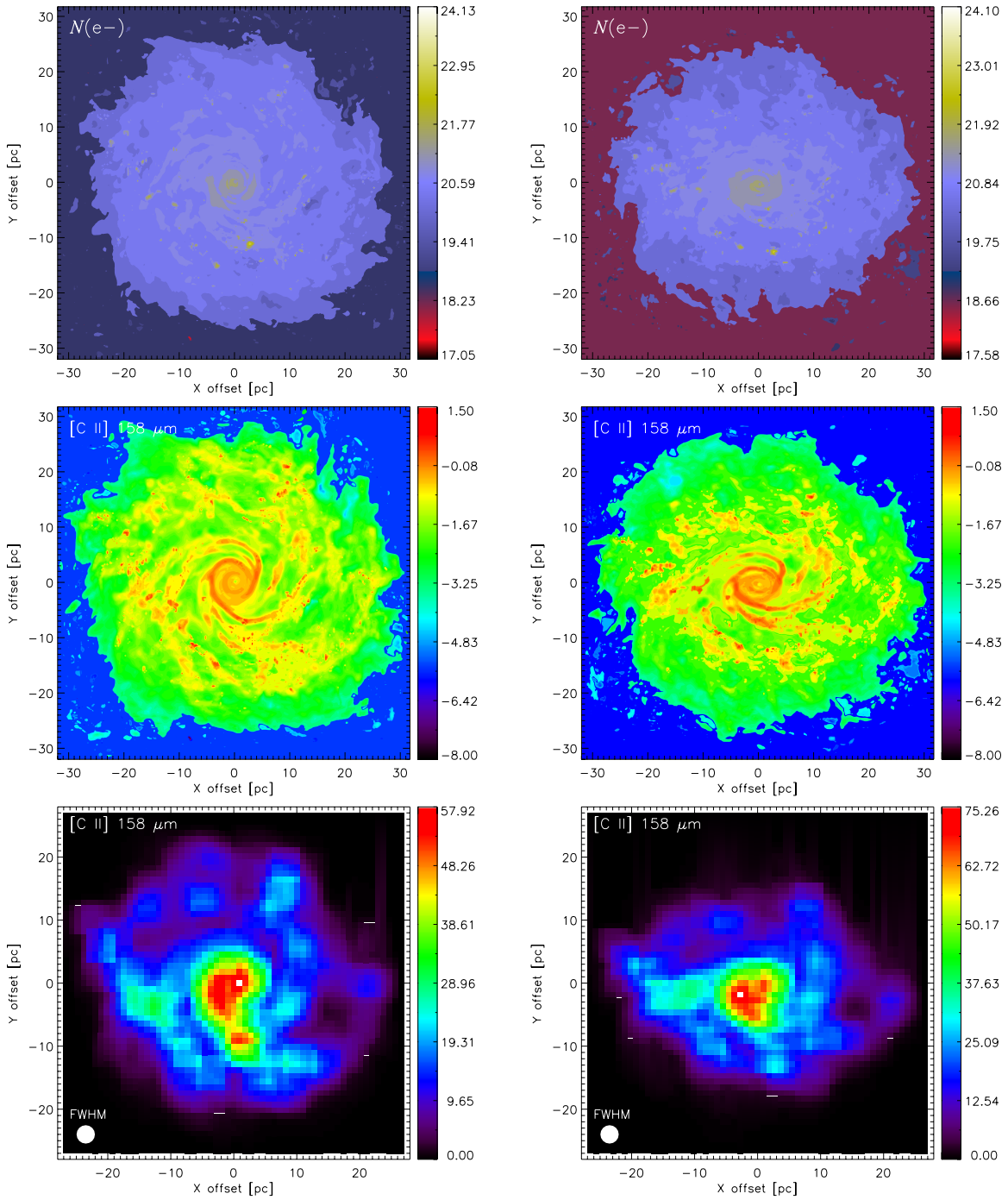

Figure 8. Left panels: face-on view (from top to bottom) of the total column density $N(e^-)$ (cm^{-2}) of electrons in logarithmic scale, the face-on view of the surface brightness (in $\log_{10}$ scale and units of erg s^{-1} cm^{-2} sr^{-1}) of the [C II] 158 μm emission, and the same map as above but convolved with a single dish beam of FWHM = 0.″15 ($\sim$ 2.8 pc at an adopted distance D = 3.82 Mpc to the source), which gives a flux in units of 10^{-15} erg s^{-1} cm^{-2}. Right panels: same as in the left panels, but with an inclination (viewing) angle of 45° about the X-axis.

(A color version of this figure is available in the online journal.)

higher than $n(H_2)_{HYD}$ is observed. This is the consequence of a weaker X-ray flux with respect to the *spherical* radiation flux. This is consistent with the fluctuations of the column density distribution of H_2 explored by WPS09 for different viewing angles, and as expected, the largest $N(H_2)$ columns are found at a viewing angle $\sim$0 degrees (i.e., edge-on). These facts imply that molecules will tend to disappear in the central ($\lesssim$10 pc) region. But, depending on the viewing angle, and for total hydrogen columns $\gtrsim 10^{24}$ cm^{-2} as in the case of, for instance, the LIRG NGC 4945, molecules can survive and emission lines like, e.g., high-J CO, [C II], [Ne II] and [Ne V], can be bright. In all, we conclude that the H_2 abundance in the AGN torus is strongly affected by the black hole ($\leqslant$10 pc) and star formation ($\geqslant$10 pc) (see also Schleicher et al. 2010).

We note, though, that the nature of the models used here to derive the temperature and density of the gas (a static

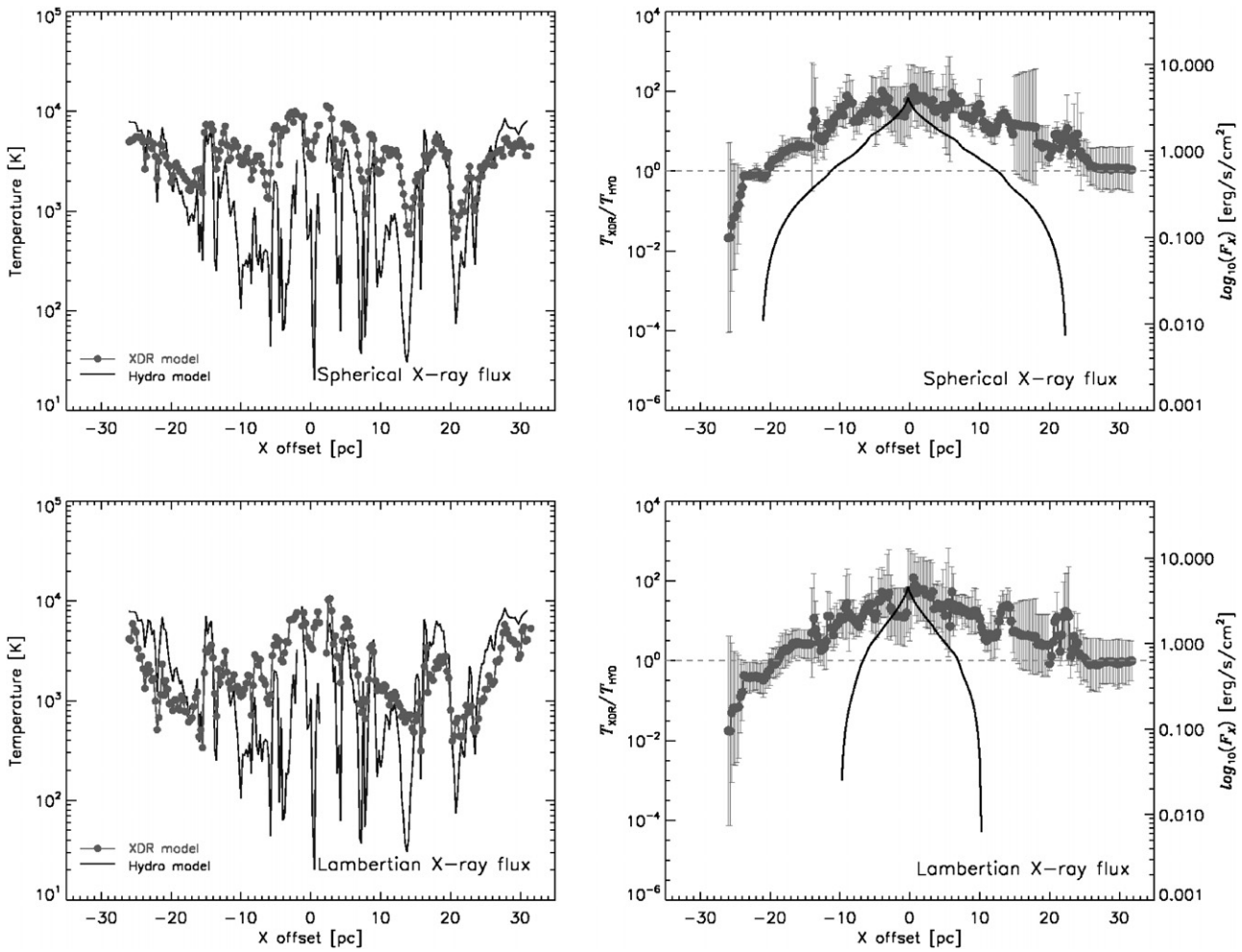

Figure 9. Top left: average temperature $T_{\rm HYD}$ (in units of K) of the gas along a $64 \times 1.25 \times 1.5$pc^3 strip volume, as estimated in the 3D hydrodynamical model (black line) and the corresponding H_2 abundance-weighted average temperature $T_{\rm XDR}$ obtained from the XDR chemical model (gray line) using the *spherical* X-ray flux (Equation (6)). The filled circles show the actual data points obtained with the XDR model in grid cells with $T_{\rm HYD} < 10^4$ K. Top right: average $T_{\rm XDR}/T_{\rm HYD}$ ratio (gray line + filled circles) and the average *spherical* X-ray flux (solid black line) F_X (erg s^{-1} cm^{-2}) in $\log_{10}$ scale. The standard deviation at each ΔX offset is shown by the error bars. The relative average temperature is directly related to the impinging flux at each grid point. The average temperature $T_{\rm XDR}$ is predominantly higher than $T_{\rm HYD}$ in the inner 20 pc around the center of the AGN torus. The dashed line indicates where $T_{\rm XDR}/T_{\rm HYD} = 1$. The bottom panels show the same as above, but for the *Lambertian* X-ray flux. The average temperature $T_{\rm XDR}$ is still higher than $T_{\rm HYD}$, but the difference is smaller than for the *spherical* X-ray flux, particularly beyond $\pm$5 pc from the central SMBH.

X-ray-driven chemical model and a hydrodynamical X-ray free model) are different, and a comparison between their corresponding derived temperatures and densities is merely intended to motivate the need for a joint XDR–hydrodynamical model for the thermodynamics of AGN tori. A first attempt to this effect has been made by Hocuk & Spaans (2010) for individual $\sim$1 pc molecular clouds close to an SMBH.

4. FINAL REMARKS

We compared the total hydrogen column density, N(CO) and CO $J = 1 \rightarrow 0$ to $J = 9 \rightarrow 8$ line intensities, and found that the mid-J CO lines are excellent probes of density and dynamics, but the low-J CO lines are not good tracers of $n_{\rm H}$ in the central ($\lesssim$60 pc) region of the AGN torus. The analysis of the $X_{\rm CO}/\alpha$ conversion factors indicated that only the higher J CO lines will show a linear correlation with the gas mass in AGN tori at lower spatial resolutions ($\sim$9 pc). But at higher resolution ($<$5 pc), different proportionality factors (or no correlation at all) appear between the CO lines and the total gas mass in AGN tori. We also determined that the [C II] 158 μm emission will trace mostly the central region of AGN tori, detectable (but not resolved) by ALMA in $z \gtrsim 1$ galaxy nuclei.

We found that the presence of X-rays has an undeniable effect on the thermodynamics of the AGN torus, up to at least 60 pc. An important implication of this is that circumnuclear star formation could be suppressed in the central $\sim$5 pc. This can shed light on the starburst–AGN connection. Self-consistent UV/X-ray radiation-chemical-hydrodynamical simulations (e.g., Hocuk & Spaans 2010) will allow us to explore this theoretically, and their predictions can be confirmed (and used for data interpretation) by ALMA in the near future.

With a rest frequency of 691.5 GHz, the CO $J = 6 \rightarrow 5$ line can be observed with the ALMA band nine receivers, which will be the highest frequency band available when the early science begins with $\geqslant$16 antennas. Considering a minimum baseline of

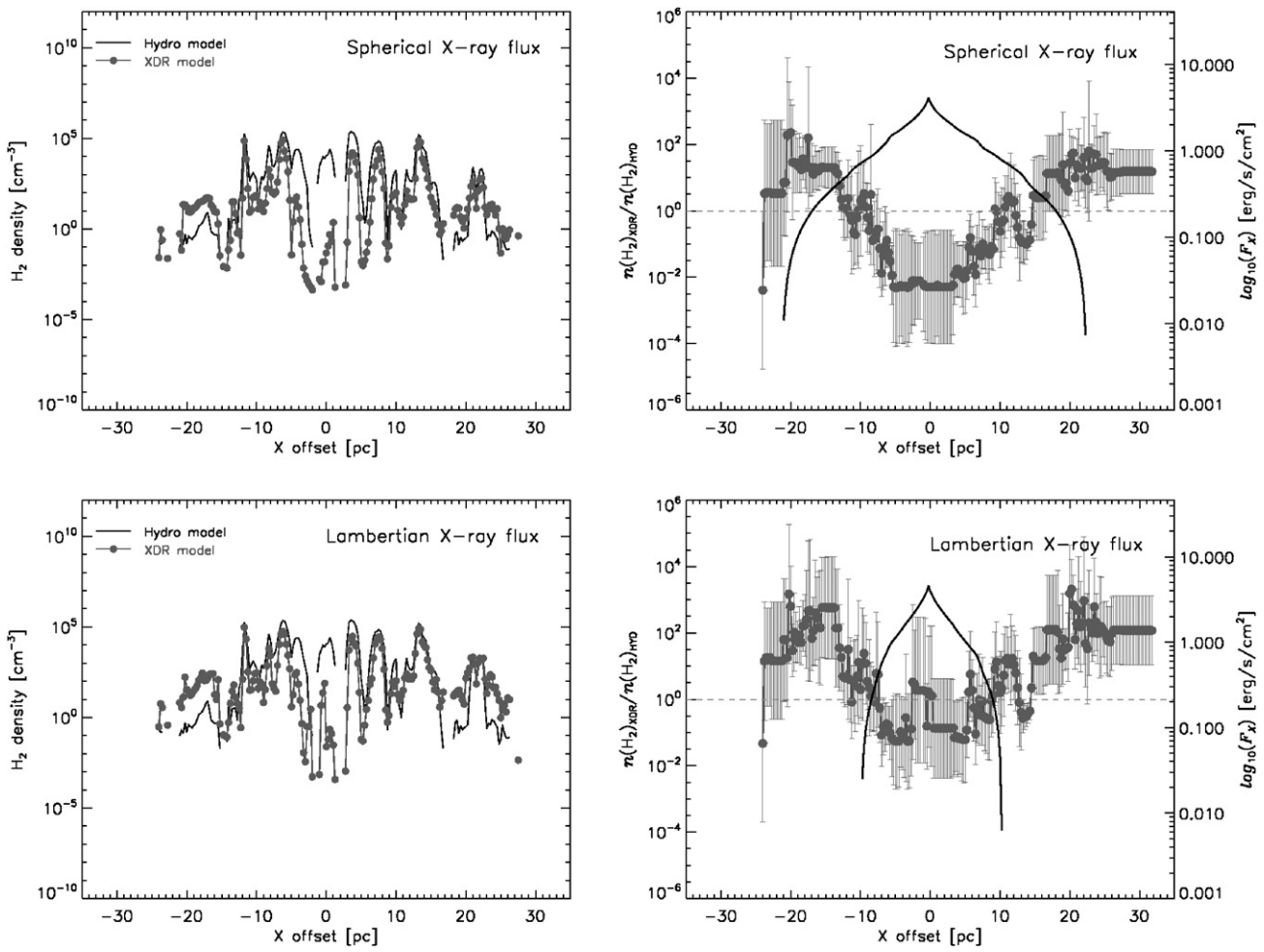

Figure 10. Top left: average density of molecular hydrogen $n(H_2)_{HYD}$ (in units of cm^{-3}) of the gas along a $64 \times 1.25 \times 1.5 pc^3$ strip volume, as estimated in the 3D hydrodynamical model (solid line) and the corresponding average $n(H_2)_{XDR}$ density obtained from the XDR chemical model (gray line + filled circles) using the *spherical* X-ray flux (Equation (6)). The filled circles show the actual data points obtained with the XDR model in grid cells with $T_{HYD} < 10^4$ K. Top right: average $n(H_2)_{XDR}/n(H_2)_{HYD}$ ratio (gray line + filled circles) and the average *spherical* X-ray flux (solid black line) F_X (erg s^{-1} cm^{-2}) in $\log_{10}$ scale. The standard deviation of the relative density at each ΔX offset is shown by the error bars. The dashed line shows where $n(H_2)_{XDR}/n(H_2)_{HYD} = 1$. The bottom panels show the same as above, but for the *Lambertian* X-ray flux. The turnover in the relation of the hydrogen density is still at about $\Delta X = 10$ pc from the central SMBH, but $n(H_2)_{XDR}$ can be up to 10^3 times higher than for the *spherical* X-ray flux beyond ± 10 pc.

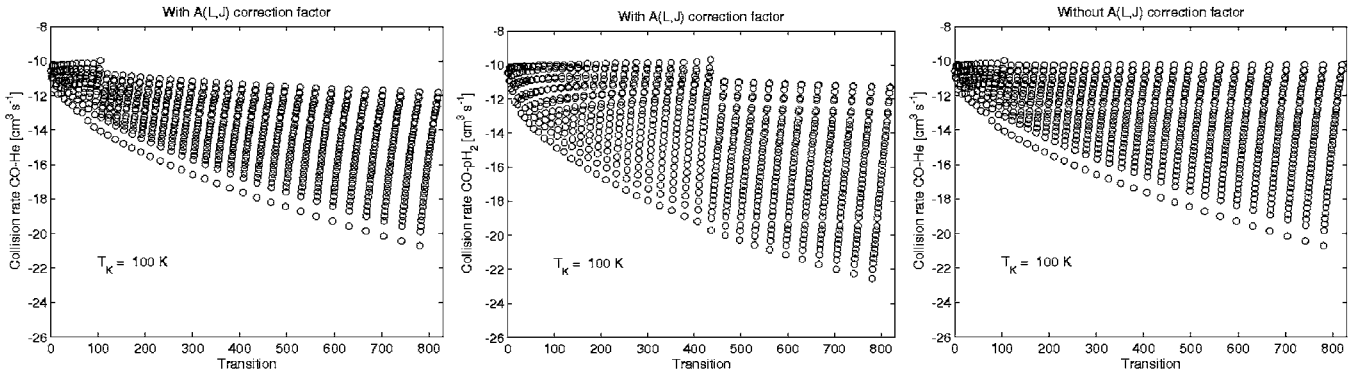

Figure 11. Top left panel: collisional rate coefficients (cm^3 s^{-1}) for CO with para-H_2 as collision partner. Top right panel: collisional rate coefficients for CO colliding with He with the wrong Wigner 3-*j* function. Bottom panel: collisional rate coefficients for CO–He collision partners with the correct Wigner 3-*j* function.

250 m for the compact configuration, we would have an angular resolution[8] of FWHM $\approx 0\farcs35$ that will allow us to resolve structures of ∼7 pc at a nearby distance of 4 Mpc (about the distance to NGC 4945) and of ∼25 pc at a distance of 15 Mpc (roughly the distance to NGC 1068). In the near future, however, the higher sensitivity (with ⩾50 antennas) and the availability of longer baselines of up to ∼15 km will provide angular resolutions of FWHM $\approx 0\farcs006$ with ALMA band nine, which will allow the study of structures between ∼0.1 pc and ∼0.4 pc,

[8] http://science.nrao.edu/alma/earlyscience.shtml

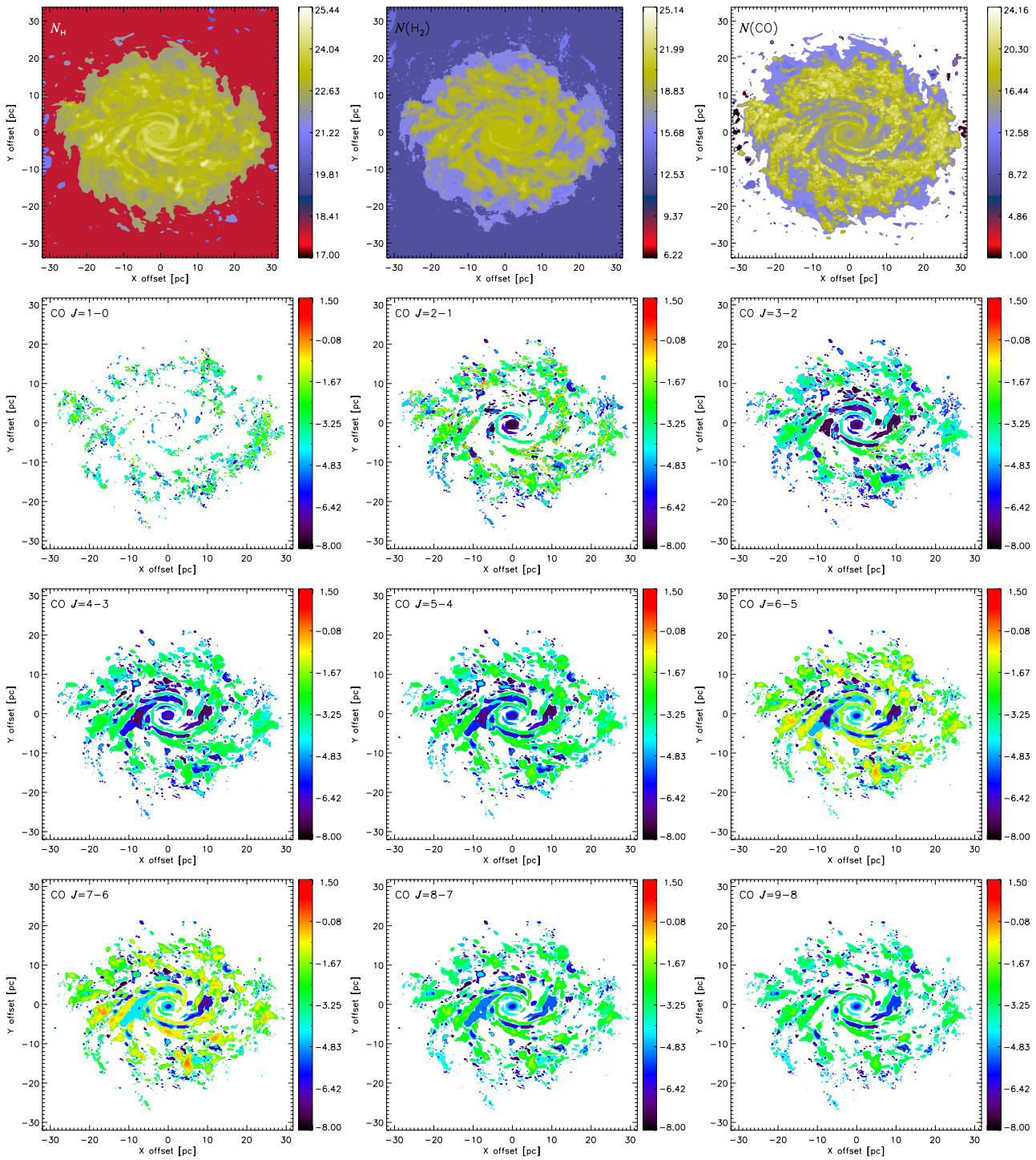

Figure 12. Top panels: maps with a 45° inclination about the X-axis of the total column density (units of cm^{-2}) N_{H} (left), the column density of molecular hydrogen $N(\mathrm{H}_2)$ (middle), and the CO column $N(\mathrm{CO})$ (right) in logarithmic scale. Bottom panels: surface brightness maps of the $J = 1 \rightarrow 0$ to $J = 9 \rightarrow 8$ transitions of CO (in $\log_{10}$ scale and units of $\mathrm{erg\,s^{-1}\,cm^{-2}\,sr^{-1}}$), as observed at the surface of the face-on data cube. The larger columns seen through the line of sight with the 45° inclination produce higher emissions of the CO transitions with respect to the face-on maps of Figure 4. However, the higher CO lines (from $J = 4 \rightarrow 3$ up to $J = 9 \rightarrow 8$) are still better tracers of the inner region of the torus.

(A color version of this figure is available in the online journal.)

respectively, at the distances mentioned above. Therefore, the spatial scales ($\geqslant$0.25 pc) that we probe with our simulations match the angular resolutions provided by ALMA.

We thank the referee for his/her constructive and insightful remarks that helped to improve this work. We are grateful to Aycin Aykutalp and Seyit Hocuk for their help and advise in using the Gemini supercomputers at the Kapteyn Institute. We are also thankful to Dieter Poelman for initial discussions and help with the original $\beta 3D$ radiative transfer code. Molecular Databases that have been helpful include the NASA/JPL, LAMDA, and NIST. The hydrodynamical model was computed on NEC SX-9 at Center for Computational Astrophysics, CfCA, of National Astronomical Observatory of Japan. The radiative trans-

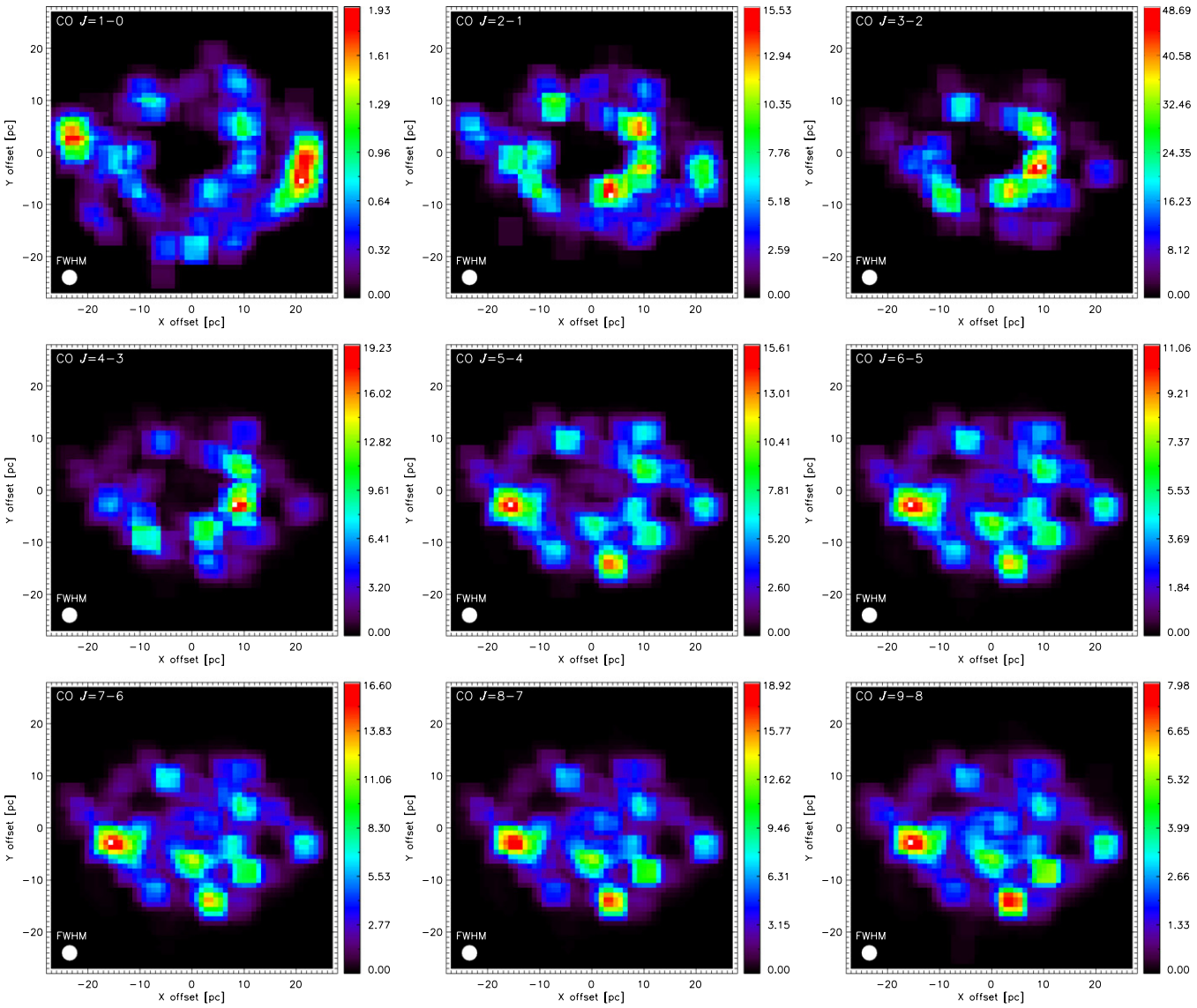

Figure 13. Maps of the flux (erg s^{-1} cm^{-2}) of the CO transitions (from $J = 1 \rightarrow 0$ to $J = 9 \rightarrow 8$) with a 45° inclination about the *X*-axis and convolved with a single dish beam of FWHM = 0.″15 (∼2.8 pc). We adopt a distance $D = 3.82$ Mpc to the source. Although the $J = 3 \rightarrow 2$ transition does not trace the warmer gas of the inner NLR, it is the brightest emission line of this configuration (see the color scale).

(A color version of this figure is available in the online journal.)

fer and line tracing models were computed on Cray SV1e at the Centre for High Performance Computing and Visualisation, HPC/V, University of Groningen, The Netherlands.

APPENDIX A

ROTATIONAL EXCITATION OF CO BY He

We used the rate coefficients for pure rotational de-excitation of CO by collisions with He atoms reported in Cecchi-Pestellini et al. (2002). The original rate coefficients are given for the first 15 rotational levels and for 10 different temperatures from 5 to 500 K. In order to extend the available rates to higher rotational levels and temperatures, we followed the methodology for linear molecules described by Schöier et al. (2005), which was used to produce the LAMDA database.

We first extrapolated the downward collisional rate coefficients ($\Delta J = J_u \rightarrow J_l$, $J_u > J_l$) in temperature (up to 2000 K) using the modified version of the analytic approximation given by de Jong et al. (1975) and presented by Bieging et al. (1998):

$$\gamma_{ul} = A(\Delta J)y \exp[-B(\Delta J)y^{1/4}] \times \exp[-C(\Delta J)y^{1/2}], \quad \text{(A1)}$$

where $y = \Delta E_{ul}/kT$ and the three parameters A, B, and C are determined by least-squares fits to the original set of Cecchi-Pestellini et al. (2002) rate coefficients for each ΔJ. Then we extrapolated the collisional rate coefficients to include higher rotational levels (up to $J = 40$) by fitting the rate coefficients (in natural logarithmic scale) connecting the ground rotational state to a second-order polynomial:

$$\ln(\gamma_{J0}) = a + bJ + cJ^2, \quad \text{(A2)}$$

with the parameters a, b, and c determined from the fit for each temperature. The infinite-order sudden (IOS) approximation (e.g., Goldflam et al. 1977) was used to calculate the whole matrix of state-to-state rate coefficients from the coefficients

connecting the ground state γ_{L0},

$$\gamma_{JJ'} = (2J'+1)\sum_{L=|J-J'|}^{L=J+J'}(2L+1)\begin{pmatrix} J & J' & L \\ 0 & 0 & 0 \end{pmatrix}^2 \gamma_{L0}, \quad \text{(A3)}$$

$$\text{where the term } \begin{pmatrix} J & J' & L \\ 0 & 0 & 0 \end{pmatrix} \quad \text{(A4)}$$

is the Wigner 3-j symbol that designates the Clebsch–Gordan coefficients (e.g., Tuzun et al. 1998 and references therein). The IOS approximation provides an accurate description of the collisional rates if the rotational energy differences are small compared to the kinetic energy of the colliding molecules. In cases where this condition is not satisfied, it is possible to approximately correct for the deviations by multiplying the summation in Equation (A3) with the adiabaticity correction factor given by Depristo et al. (1979) and McKee et al. (1982),

$$A(L,J) = \frac{6+(\alpha L)^2}{6+(\alpha J)^2}, \text{ with } \alpha = 0.13 B_0 l \left(\frac{\mu}{T}\right)^{1/2}, \quad \text{(A5)}$$

where B_0 is the rotational constant of the colliding molecule in cm^{-3} ($B_0 = 1.9225\,\mathrm{cm}^{-3}$ for CO), $l = 3$ Å is a typical scattering length, μ is the reduced mass of the colliding system in amu ($\mu \approx 3.5$ amu for CO-He), and T is the kinetic temperature.

However, the $A(L, J)$ correction factor should be used only if $E_L > E_J$ and $(E_L - E_J) \gg E_K$, where $E_{J,L}$ is the energy of the CO rotational levels L, J, and E_K is the kinetic energy of the collision partners. The top left panel of Figure 11 shows the deviations introduced by the $A(L, J)$ factor when used arbitrarily to extrapolate the rate coefficients of CO colliding with He. The top right panel of Figure 11 shows similar discontinuities in the extrapolated rate coefficients between CO and para-H_2 presented in the current LAMDA molecular data. Similar deviations are observed for ortho-H_2. This means that the extrapolated LAMDA molecular data for CO need to be corrected. Although, the original CO–H_2 rate coefficients obtained from Flower (2001) and Wernli et al. (2006) go up to $J = 29$, and since we do not explore CO transitions above $J = 20$ we can still use the LAMDA molecular data without corrections.

In the case of the CO–He colliding system the conditions for using the $A(L, J)$ adiabaticity factor are not satisfied for the temperatures and energy levels considered here, and the IOS approximation given by Equation (A3) yields results with 10%–15% accuracy (Goldflam et al. 1977). The final extrapolated rate coefficients used in this work for the system CO–He are shown in the bottom panel of Figure 11.

APPENDIX B

CO MAPS AT 45° INCLINATION

Figures 12 and 13 show CO maps at 45° inclination.

REFERENCES

Aalto, S., Spaans, M., Wiedner, M. C., & Hüttemeister, S. 2007, A&A, 464, 193
Baan, W. A., Loenen, A. F., & Spaans, M. 2010, A&A, 516, A40
Ballantyne, D. R. 2008, ApJ, 685, 787
Bieging, J. H., Knee, L. B. G., Latter, W. B., & Olofssson, H. 1998, A&A, 339, 811
Cecchi-Pestellini, C., Bodo, E., Balakrishnan, N., & Dalgarno, A. 2002, ApJ, 571, 1015
Dame, T. M., Hartmann, D., & Thaddeus, P. 2001, ApJ, 547, 792
de Jong, T., Dalgarno, A., & Chu, S.-I. 1975, ApJ, 199, 69
Depristo, A. E., Augustin, S. D., Ramaswamy, R., & Rabitz, H. 1979, J. Chem. Phys., 71, 850
Dickman, R. L., Snell, R. L., & Schloerb, F. P. 1986, ApJ, 309, 326
Downes, D., & Solomon, P. M. 1998, ApJ, 507, 615
Downes, D., Solomon, P. M., & Radford, S. J. E. 1993, ApJ, 414, L13
Ferrarese, L., & Merritt, D. 2000, ApJ, 539, L9
Flower, D. R. 2001, MNRAS, 328, 147
Flower, D. R., & Launay, J. M. 1977, J. Phys. B: At. Mol. Phys., 10, 3673
García-Burillo, S., Combes, F., Usero, A., & Graciá-Carpio, J. 2007, New Astron. Rev., 51, 160
García-Burillo, S., Combes, F., Usero, A., & Graciá-Carpio, J. 2008, J. Phys. Conf. Ser., 131, 012031
Goldflam, R., Kouri, D. J., & Green, S. 1977, J. Chem. Phys., 67, 4149
Graham, A. W., Erwin, P., Caon, N., & Trujillo, I. 2001, ApJ, 563, L11
Häring, N., & Rix, H. 2004, ApJ, 604, L89
Henkel, C., Jacq, T., Mauersberger, R., Menten, K. M., & Steppe, H. 1987, A&A, 188, L1
Hocuk, S., & Spaans, M. 2010, A&A, 510, A110
Hogerheijde, M. R., & van der Tak, F. F. S. 2000, A&A, 362, 697
Hollenbach, D. J., & Tielens, A. G. G. M. 1999, Rev. Mod. Phys., 71, 173
Hopkins, P. F., Cox, T. J., Kereš, D., & Hernquist, L. 2008, ApJS, 175, 390
Hopkins, P. F., Hernquist, L., Cox, T. J., Robertson, B., & Springel, V. 2006, ApJS, 163, 50
Imanishi, M., Dudley, C. C., & Maloney, P. R. 2006a, ApJ, 637, 114
Imanishi, M., & Nakanishi, K. 2006, PASJ, 58, 813
Imanishi, M., Nakanishi, K., & Kohno, K. 2006b, AJ, 131, 2888
Imanishi, M., & Wada, K. 2004, ApJ, 617, 214
Kaspi, S., Smith, P. S., Netzer, H., Maoz, D., Jannuzi, B. T., & Giveon, U. 2000, ApJ, 533, 631
Kohno, K. 2005, in AIP Conf. Ser. 783, The Evolution of Starbursts, ed. S. Hüttmeister, E. Manthey, D. Bomans, & K. Weis (Melville, NY: AIP), 203
Kohno, K., Matsushita, S., Vila-Vilaró, B., Okumura, S. K., Shibatsuka, T., Okiura, M., Ishizuki, S., & Kawabe, R. 2001, in ASP Conf. Ser. 249, The Central Kiloparsec of Starbursts and AGN: The La Palma Connection, ed. J. H. Knapen, J. E. Beckman, I. Shlosman, & T. J. Mahoney (San Francisco, CA: ASP), 672
Kohno, K., Nakanishi, K., & Imanishi, M. 2007, in ASP Conf. Ser. 373, The Central Engine of Active Galactic Nuclei, ed. L. C. Ho & J.-W. Wang (San Francisco, CA: ASP), 647
Launay, J., & Roueff, E. 1977, J. Phys. B: At. Mol. Phys., 10, 879
Levenson, N. A., Sirocky, M. M., Hao, L., Spoon, H. W. W., Marshall, J. A., Elitzur, M., & Houck, J. R. 2007, ApJ, 654, L45
Levenson, N. A., Weaver, K. A., & Heckman, T. M. 2001, ApJ, 550, 230
Loenen, A. F., Spaans, M., Baan, W. A., & Meijerink, R. 2008, A&A, 488, L5
Madejski, G. M., et al. 1995, ApJ, 438, 672
Magorrian, J., et al. 1998, AJ, 115, 2285
Maloney, P. R., Hollenbach, D. J., & Tielens, A. G. G. M. 1996, ApJ, 466, 561
Martín, S., Mauersberger, R., Martín-Pintado, J., García-Burillo, S., & Henkel, C. 2003, A&A, 411, L465
McKee, C. F., Storey, J. W. V., Watson, D. M., & Green, S. 1982, ApJ, 259, 647
Meijerink, R., & Spaans, M. 2005, A&A, 436, 397
Meijerink, R., Spaans, M., & Israel, F. P. 2007, A&A, 461, 793
Narayanan, D., Cox, T. J., Hayward, C. C., Younger, J. D., & Hernquist, L. 2009, MNRAS, 400, 1919
Narayanan, D., Hayward, C. C., Cox, T. J., Hernquist, L., Jonsson, P., Younger, J. D., & Groves, B. 2010, MNRAS, 401, 1613
Narayanan, D., et al. 2008a, ApJS, 174, 13
Narayanan, D., et al. 2008b, ApJS, 176, 331
Nguyen-Q-Rieu , Henkel, C., Jackson, J. M., & Mauersberger, R. 1991, A&A, 241, L33
Ohsuga, K., & Umemura, M. 2001a, A&A, 371, 890
Ohsuga, K., & Umemura, M. 2001b, ApJ, 559, 157
Pérez-Beaupuits, J. P., Aalto, S., & Gerebro, H. 2007, A&A, 476, 177
Pérez-Beaupuits, J. P., Spaans, M., Hogerheijde, M. R., Güsten, R., Baryshev, A., & Boland, W. 2010, A&A, 510, A87
Pérez-Beaupuits, J. P., Spaans, M., van der Tak, F. F. S., Aalto, S., García-Burillo, S., Fuente, A., & Usero, A. 2009, A&A, 503, 459
Poelman, D. R., & Spaans, M. 2005, A&A, 440, 559
Poelman, D. R., & Spaans, M. 2006, A&A, 453, 615

Pounds, K. A., Nandra, K., Stewart, G. C., George, I. M., & Fabian, A. C. 1990, Nature, 344, 132
Schleicher, D. R. G., Spaans, M., & Klessen, R. S. 2010, A&A, 513, A7
Schöier, F. L., van der Tak, F. F. S., van Dishoeck, E. F., & Black, J. H. 2005, A&A, 432, 369
Solomon, P. M., & Barrett, J. W. 1991, in IAU Symp. 146, Dynamics of Galaxies and Their Molecular Cloud Distributions, ed. F. Combes & F. Casoli (Cambridge: Cambridge Univ. Press), 235
Solomon, P. M., Downes, D., Radford, S. J. E., & Barrett, J. W. 1997, ApJ, 478, 144
Solomon, P. M., Rivolo, A. R., Barrett, J., & Yahil, A. 1987, ApJ, 319, 730
Soltan, A. 1982, MNRAS, 200, 115
Spaans, M., & Meijerink, R. 2008, ApJ, 678, L5
Strong, A. W., & Mattox, J. R. 1996, A&A, 308, L21
Tacconi, L. J., et al. 2008, ApJ, 680, 246
Tuzun, R. E., Burkhardt, P., & Secrest, D. 1998, Comput. Phys. Commun., 112, 112
Usero, A., García-Burillo, S., Fuente, A., Martín-Pintado, J., & Rodríguez-Fernández, N. J. 2004, A&A, 419, 897
van der Tak, F. F. S., Black, J. H., Schöier, F. L., Jansen, D. J., & van Dishoeck, E. F. 2007, A&A, 468, 627
van der Werf, P. P., et al. 2010, A&A, 518, L42
Verner, D. A., & Yakovlev, D. G. 1995, A&AS, 109, 125
Wada, K., & Norman, C. A. 2002, ApJ, 566, L21 (WN02)
Wada, K., Papadopoulos, P. P., & Spaans, M. 2009, ApJ, 702, 63 (WPS09)
Wada, K., & Tomisaka, K. 2005, ApJ, 619, 93 (WT05)
Wernli, M., Valiron, P., Faure, A., Wiesenfeld, L., Jankowski, P., & Szalewicz, K. 2006, A&A, 446, 367
Wilson, N. J., & Bell, K. L. 2002, MNRAS, 337, 1027
Yamada, M., Wada, K., & Tomisaka, K. 2007, ApJ, 671, 73 (YWT07)
Zdziarski, A. A., Johnson, W. N., Done, C., Smith, D., & McNaron-Brown, K. 1995, ApJ, 438, L63